2.5-D Local Hybrid Simulations of Hot Flow Anomalies Under

2	Various Magnetic Field Geometries
3	
4	Andrew Vu ¹ , Terry Z. Liu ¹ , Vassilis Angelopoulos ¹ , and Hui Zhang ²
5	
6	¹ Department of Earth, Planetary, and Space Sciences, University of California, Los Angeles,
7	Los Angeles, CA, USA. ² Geophysical Institute, University of Alaska Fairbanks, Fairbanks, AK,
8	USA.
9	
10	
11	Corresponding Author: Terry Z. Liu (terryliuzixu@ucla.edu)
12	
13	Key Points
14	• We conduct 2.5D local hybrid simulations to study the formation of hot flow
15	anomalies under various magnetic field geometries.
16	• Foreshock ions from one side drive current on the other side of discontinuity, which
17	determines hot flow anomaly profiles.
18	• At quasi-perpendicular shocks, ions leak from the sheath and travel upstream along
19	the discontinuity to jumpstart the formation process.
20	Abstract
21	Hot flow anomalies (HFAs) are ion kinetic phenomena that play an important role in
22	geoeffects and particle acceleration. They form due to the currents driven by demagnetized

foreshock ions around a tangential discontinuity (TD). To understand the profile of such currents around a TD with foreshock ions on both sides, we use 2.5-D local hybrid simulations of TDs, interacting with a planar shock with various shock geometries. We find that the electric field direction relative to the TD plane provides information about how the foreshock ion-driven currents affect the magnetic field around the TD. For TDs embedded in the quasi-parallel shock on both sides, the foreshock ions from one side of TD can cross it determining the current profile on the other side. In contrast, for TDs embedded in the quasi-perpendicular shock, sheath-leaked ions enter the TD and determine the current profile. We find that the foreshock ULF waves can periodically modulate how foreshock ions interact with the TD and thus the current profile. Studying the effects of various magnetic field configurations allows us to build a more comprehensive model of HFA formation.

1 Introduction

When the interplanetary magnetic field (IMF) is nearly parallel with the bow shock normal, also known as the quasi-parallel bow shock, incoming solar wind particles can become reflected at the bow shock and travel back upstream to populate a region known as the foreshock (e.g., Eastwood et al., 2005). At the foreshock, backstreaming ions, or foreshock ions, can interact with the solar wind ions and discontinuities to form transient kinetic phenomena known as foreshock transients (see review by Zhang et al., 2022). In spacecraft observations, these foreshock transients can exhibit greatly deflected plasma bulk flows and increased plasma pressures within a density and magnetic field strength-depleted core. One type of foreshock transients, hot flow anomalies (HFAs), is characterized by the presence of two density and magnetic field strength-enhanced boundaries (compressional boundaries or shocks) bounding the depleted core (e.g., Schwartz et

al., 1985, 2018). Observed HFAs expand on two sides with spatial scales of 1-3 R_E (e.g., Facskó et al., 2009). Because of their low-dynamic pressure cores, HFAs can deform the local bow shock surface and disturb the magnetosphere and ionosphere (e.g., Sibeck et al., 1999; Jacobsen et al., 2009; Hartinger et al., 2013; Archer et al., 2014, 2015; Wang B. et al., 2020, 2021). In addition, HFAs can participate in the acceleration of particles at the bow shock (e.g., Wilson et al., 2016; Liu et al., 2016, 2017, 2018, 2019, 2020a; Turner et al., 2018; Omidi et al., 2021).

46

47

48

49

50

51

52

53

54

55

56

57

58

59

60

61

62

63

64

65

66

67

68

Understanding the detailed formation mechanism of HFAs is still an ongoing endeavor. In early hybrid simulations, tangential discontinuities (TDs) in the solar wind can cause the build-up and thermalization of backstreaming particles, as the TDs convect along the bow shock surface (Thomas et al., 1991; Lin, 1997, 2002; Omidi and Sibeck, 2007). Archer et al. (2015) and Liu et al. (2015) explain that when foreshock ions experience a sudden change in the magnetic field, a portion of their initial parallel speed is projected into the new perpendicular direction, increasing their thermal energy. Because there is a reduction of their parallel speeds, this leads to the local accumulation of foreshock ions because of mass flux conservation. The enhancement in the density and thermal energy leads to an increase in the thermal pressure that forms a low-density core bounded by compressional boundaries or shocks. However, this description still needs to be more accurate and quantitative. Thermal pressure is not applicable when the foreshock ion gyroperiods (of 10 to 20 seconds) are comparable to the formation time scales of HFAs, and the foreshock ion gyroradii (of the order of 1000 km) are larger than or comparable to the size of solar wind discontinuities. Therefore, properly describing the formation of HFAs involves treating foreshock ions as kinetic particles.

An et al. (2020) using particle-in-cell simulations and Liu et al. (2020b) using spacecraft observations presented evidence for a plasma-physical formation model of foreshock transients

involving the kinetic effects of ions. In their model, foreshock ions become demagnetized when they interact with a discontinuity. As the electrons remain magnetized, a Hall current is generated that changes the magnetic field of, and around, the discontinuity. These magnetic field variations induce an electric field that compels the cold plasma to undergo an E×B drift outward, away from the discontinuity, i.e., an expansion. This results in the characteristic depleted core and compressional boundaries or shocks. In the formation process, the foreshock ions performing a partial gyration against the induced electric field provide the energy required for the expansion of the structure.

Previous studies using the injection of a fixed distribution of foreshock ions have revealed that the thickness of a TD determines whether one or two compressional boundaries form around a TD (Vu et al., 2022) and that the distribution and properties of the injected foreshock ions can also influence the formation and expansion of foreshock transients (Vu et al., 2023). These simulation results have established several analytical models (Liu et al., 2023a, 2023b, 2023c). However, these simulations and models only considered a simple geometry: TDs with quasiparallel conditions or an ion foreshock on only one side. In observations, HFAs are frequently embedded in the foreshock and occasionally in the quasi-perpendicular region on both sides (e.g., Zhang et al., 2010; Wang et al., 2013). The profile of a foreshock ion-driven current under these geometries remains to be determined; such an understanding is critical to establishing more advanced models. Thus, this paper aims to explore how the formation of HFAs varies under different magnetic field configurations and shock conditions through local hybrid simulations of a planar shock – the simulated shock is key to generate more realistic foreshock ion populations (rather than injecting fixed distributions from a simulation boundary).

In this paper, we use 2.5-D local hybrid simulations of a planar shock to compare the formation differences of HFAs in different magnetic field configurations. We introduce the hybrid code and describe the initial simulation setup in Section 2. Section 3 presents the simulation results of HFAs formed under various magnetic field configurations. Section 4 discusses the importance and connection between the magnetic field configuration and the foreshock ion properties for the variation of HFA formations. In Section 5, we conclude and discuss our results.

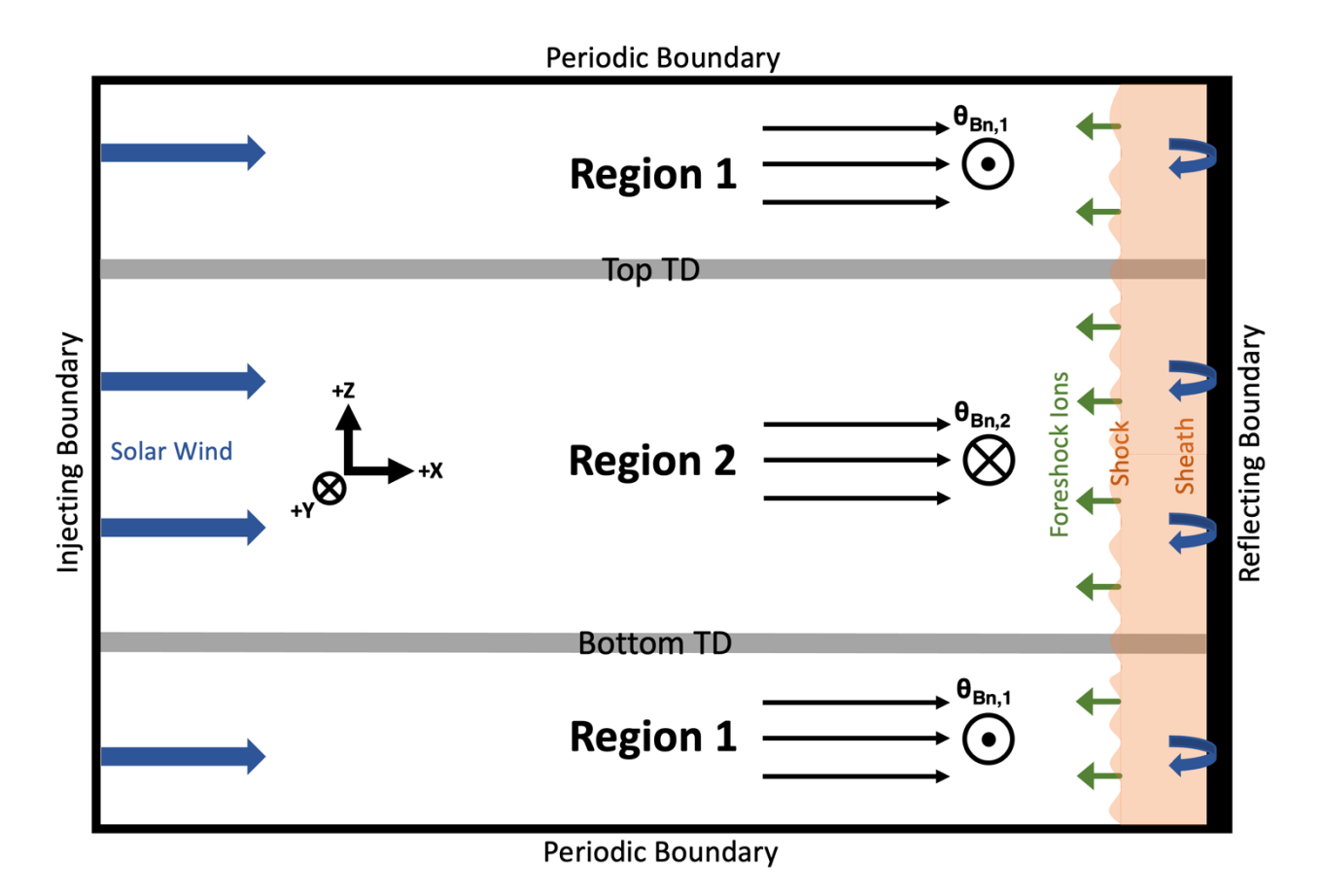


Figure 1 – Diagram showing the simulation setup with a solar wind ion injecting boundary on the left and a solar wind ion reflecting boundary on the right. A shock is formed ahead of the reflecting boundary, and foreshock ions are generated upstream of the shock. The Bottom and Top TDs change the out-of-the-plane By magnetic field direction across them. The Bottom TD is

focused which generates HFAs, whereas the Top TD is examined in the accompanying paper (Vu et al. submitted to JGR).

2 Method

To model the interaction of a tangential discontinuity with a planar shock, we use a local 2.5-D hybrid simulation code with kinetic ions and fluid electrons originally written by Swift (1995, 1996), Delamere et al. (1999), and Delamere (2006, 2009) and modified from Vu et al. (2022, 2023). The code assumes quasi-neutrality, is non-radiative, and has electrons represented as a massless and charge-neutralizing fluid. The ion particle motion for each cloud-in-cell macroparticle is determined by:

111
$$\frac{d\mathbf{v}}{dt} = \mathbf{E} + \mathbf{V} \times \mathbf{B} - \nu(\mathbf{u}_{i} - \mathbf{u}_{e}),$$

where \mathbf{E} is electric field in units of ion acceleration, \mathbf{B} is magnetic field in units of gyrofrequency, ν is the collision frequency between ions and electrons, \mathbf{V} is fluid velocity, and \mathbf{u}_i and \mathbf{u}_e are the ion and electron bulk velocities. The electric field is calculated through a combination of the electron momentum equation and Ampere's law,

116
$$\mathbf{E} = -\mathbf{u}_{e} \times \mathbf{B} - \nu(\mathbf{u}_{e} - \mathbf{u}_{i}) = -\left(\mathbf{u}_{i} - \frac{\nabla \times \mathbf{B}}{\alpha n}\right) \times \mathbf{B} - \nu \frac{\nabla \times \mathbf{B}}{\alpha n},$$

where n is plasma density, $\alpha = \mu_0 q^2/m_p$ and m_p is the proton mass. The α parameter is used to scale the ion macro-particle densities to physical values. Faraday's law is used to advance the magnetic fields. Particle and field equations include dissipation terms for the ion-electron collisions to reduce numerical instabilities. Particle updates use a predictor-corrector scheme, and the fields are updated in sub-cycles of fractional particle time steps using the leap-frog technique. The configuration of the simulation, depicted in Figure 1, is described below.

At the left boundary, we apply an open boundary condition, facilitating the continuous injection of a cold Maxwellian distribution for the solar wind ions with a bulk flow in the +x direction. On the right boundary, a reflecting boundary condition is implemented, resulting in the x component of ion particle velocities becoming negative, –x direction, with continuous electric field and magnetic field across the boundary. This reflective boundary facilitates the emergence of a shock, a sheath, and a foreshock. The upper and lower horizontal boundaries are set as periodic boundaries.

123

124

125

126

127

128

129

130

131

132

133

134

135

136

137

138

139

140

141

142

143

144

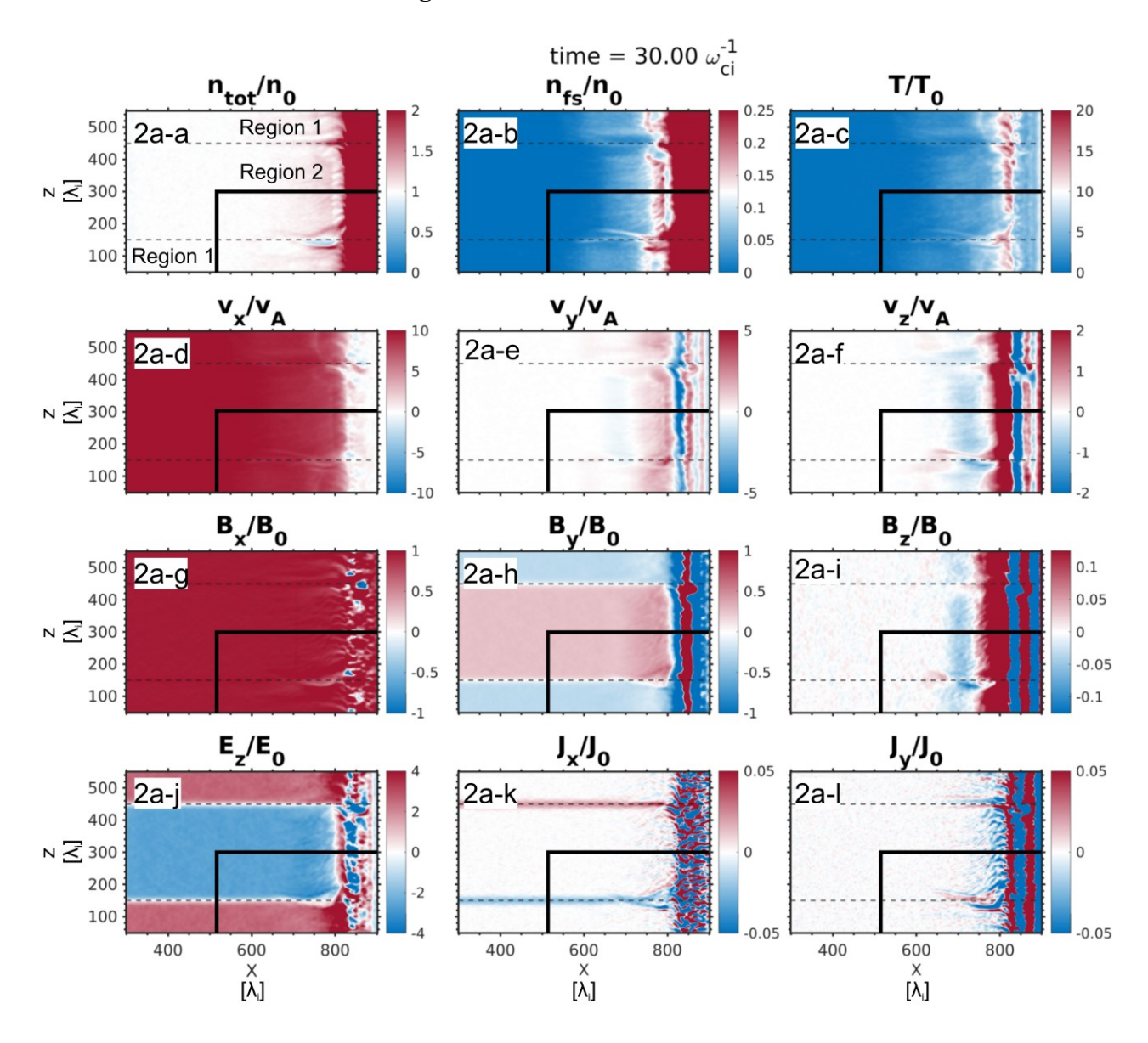
The initial field setup involves two horizontal TDs, the Bottom TD and the Top TD, with normals oriented in the z direction. The magnetic field profiles within the TDs follow Harris current sheet with slight ion density increases that balance the pressure. The Bottom and Top TDs encompass the magnetic field transition from Region 1 to Region 2 and from Region 2 back to Region 1, respectively. In Region 1 (Region 2), the magnetic fields are aligned tangentially to the TD plane, by nature, by initializing the magnetic field to the right in the +x direction and +y or -y direction (into or out of plane). The magnetic cone angle is defined here as the $\arctan(B_v/B_x)$, where B_x is set to be always positive, and thus B_y determines its sign. Because the shock normal is in the x direction and there is no B_z , the cone angle is the same as θ_{Bn} (the angle between the magnetic field and the shock normal). The thickness of the magnetic field change, or of each TD, is about 15 solar wind thermal ion gyroradii, within typical TD thickness range for HFAs (1000-3000 km; Zhao et al., 2017). We use a periodic boundary for the y direction (in and out of the page) to downgrade 3-D hybrid simulation code by setting 3 cells in the y direction. We set up a convecting vertical layer to make the shock develop uniformly in the two regions before the TDs intersect it by varying B_y across the layer (see descriptions in the supporting information).

To understand the formation of HFAs, we set up simulations under various magnetic field configurations. We categorize the magnetic field setup into two situations in which the B_y values, or the cone angles, on the two sides of the TD, have either opposite signs or the same sign. When the cone angles have opposite signs, the convection electric field (in the simulation rest frame) points either towards or away from the TD on both sides. When they have the same sign, the convection electric field points toward the TD on only one side. The direction of the convection electric field relative to the TD normal is one well-known criterion of HFAs (e.g., Schwartz et al., 2000). It is thus essential to examine the exact role of electric field direction in HFA formation.

We test the symmetric cases with the same B_y magnitude (but different signs) on the two sides of TDs. The symmetric cases involve magnetic field cone angles θ of $\pm 15^{\circ}$ and $\pm 60^{\circ}$, which cover the situations when a TD interacts with a quasi-parallel shock and a quasi-perpendicular shock. In these cases, the foreshock ion conditions are about the same on both sides of the TD, so we can focus on the role of magnetic field geometry. We also test the cases with the same B_y sign (but different magnitude) on the two sides of TDs. The asymmetric cases involve magnetic field cone angles θ of $\pm 15^{\circ}/\pm 45^{\circ}$ and $\pm 5^{\circ}/\pm 20^{\circ}$. (The case with transition from quasi-parallel shock to quasi-perpendicular shock across TDs has been examined by Vu et al. (2022; 2023).) All other simulation parameters are kept constant between every simulation run. The background magnetic field strength is ± 5.00 nT and the solar wind density is ± 5.00 cm⁻³, resulting in an Alfvénic speed ± 1.00 of ± 1.00 magnetic field strength is ± 1.00 nT and the solar wind ion bulk flow speed is ± 1.00 magnetic speed V_A of ± 1.00 magnetic field should be a simulation box spanning ± 1.00 magnetic field should be a length of an ion inertial length ± 1.00 same as solar wind thermal ion gyroradius) and ± 1.00 ion macroparticles per cell.

3 Results

3.1. Case 1 – -15° to +15° Cone Angle



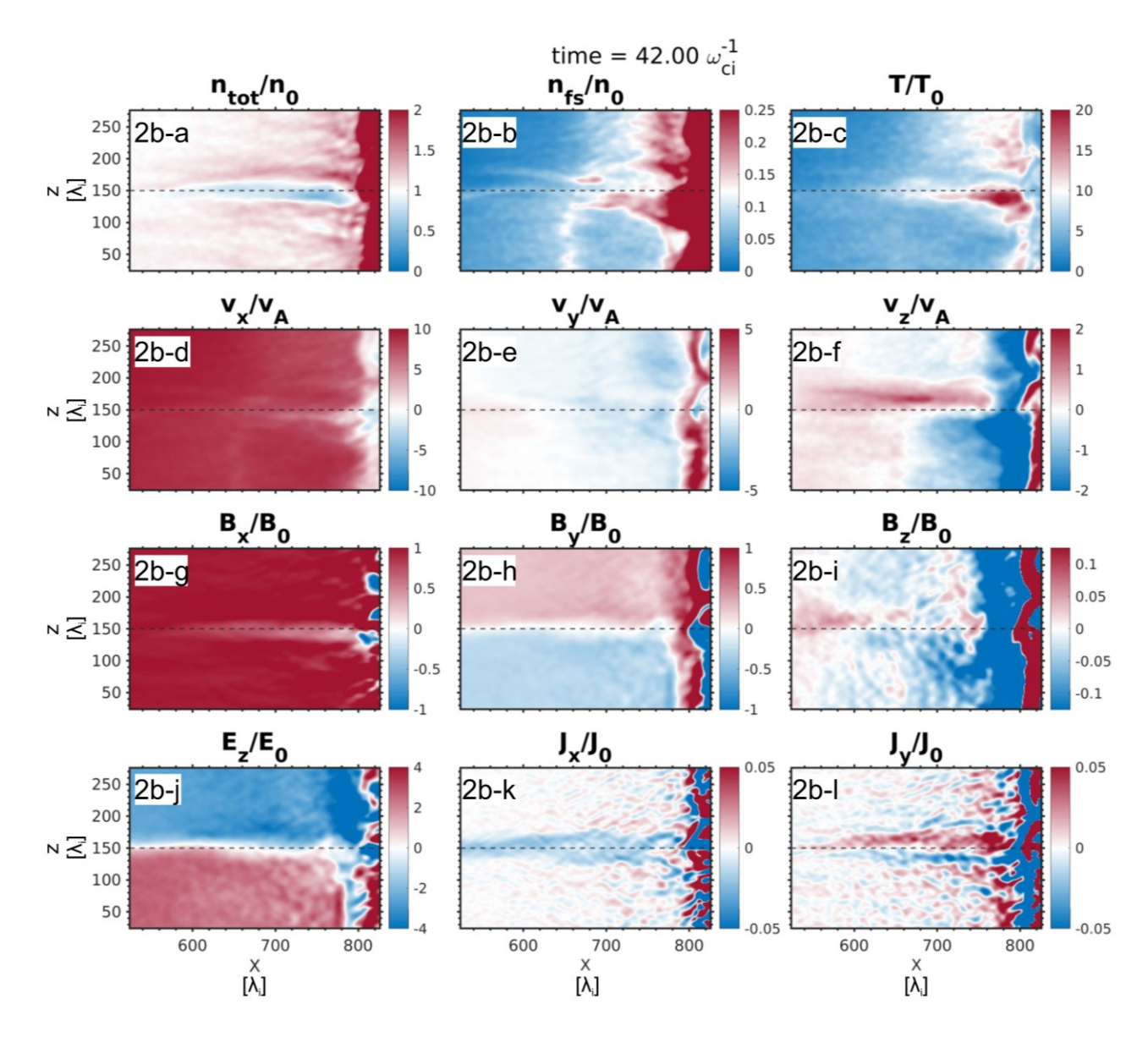


Figure 2 – 2-D simulation results for Case 1 where the cone angles vary from -15° (Region 1) to +15° (Region 2) and back to -15° (Region 1). Figure 2a shows the earlier time results at $t=30\omega_{ci}^{-1}$ (where ω_{ci} is ion gyrofrequency), and Figure 2b shows the later time results at $t=42\omega_{ci}^{-1}$ zooming in to the Bottom TD roughly corresponding to the black box in Figure 2a. Each figure shows a snapshot of (a) total densities, (b) foreshock ion densities, (c) total ion temperatures, (d)-(f) bulk flow components in x, y, and z direction, (g)-(i) magnetic field components in x, y, and z direction, (j) electric field component E_z , and (k)-(l) current density components I_x and I_y . For simplicity,

foreshock ions are categorized by negative V_x (although sheath ions are partially included, we only consider the upstream region). The horizontal dashed lines represent the positions of the Bottom and Top TDs.

We begin with a symmetric case where the TDs change the magnetic field cone angle from -15° to +15° and back to -15° (without changing solar wind field strength). This cone angle configuration allows for the generation of foreshock ions that travel upstream from the quasiparallel planar shock. Figures 2 shows the plasma densities of the solar wind and the foreshock ions, the total ion temperature, total ion bulk flow components, magnetic field components, electric field z component, and current density x and y components. Figure 2a shows simulation results at an earlier time, and Figure 2b zooms in at the Bottom TD at a later time. In Figures 2a-e and 2a-f, V_y and V_z upstream of the shock exhibit temporal variation and spatial variation along the x direction associated with B_y and B_z variation (Figures 2a-h and 2a-i). Such variation convects downstream (see Movie M1 in the supporting information) suggesting disturbances from foreshock ULF waves.

In this setup, the electric fields point toward the Bottom TD on both sides (Region 1 and Region 2) and away from the Top TD on both sides (Region 2 and Region 1) (Figure 2a-j). We see a tenuous, hot core forms at the Bottom TD (Figures 2a-a and 2a-c), which grows into an HFA elongated along the TD with small density, high temperature, flow deflection/deceleration, and small field strength (Figures 2b-a, 2b-c, 2b-d, 2b-g), bounded by two boundaries with enhanced density (Figure 2b-a). V_z shows divergence along z direction indicating expansion of the HFA (Figure 2b-f). At the Top TD, on the other hand, a small compressional boundary with enhanced

- density and field strength starts to form, which is examined in the accompanying paper (Vu et al.,
- submitted to JGR). We next focus on the formation of the HFA.

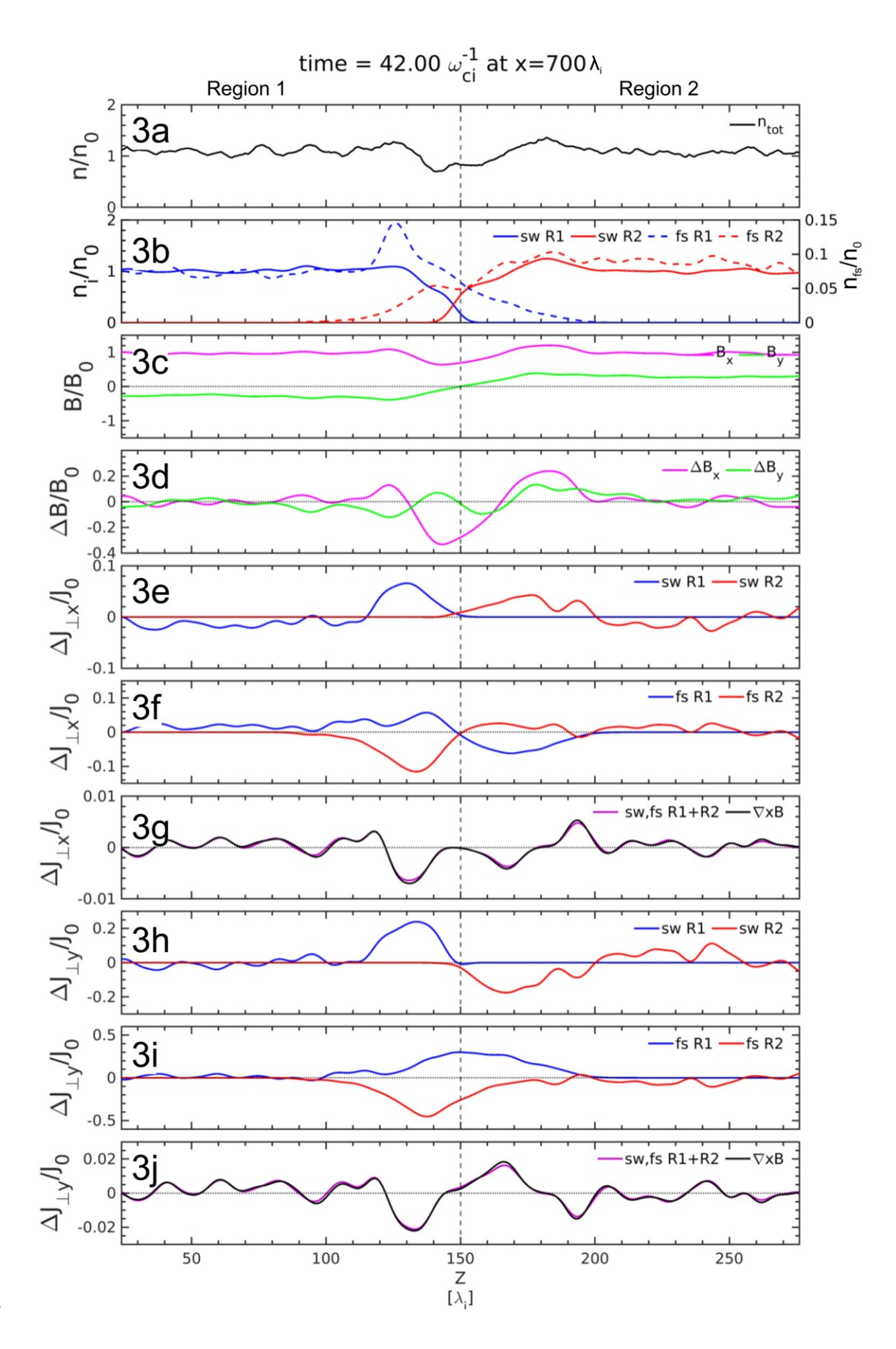


Figure 3 – 1-D cut for Case 1 for the Bottom TD at x=700 λ_i where the cone angle below the TD (Region 1) is -15° and above the TD (Region 2) is +15°, at t=42 ω_{ci}^{-1} (same as Figure 2b). The panels show (a) total ion density; (b) solar wind (sw) ion density (solid lines, corresponding to left vertical axis) and foreshock ion (fs) density (dashed lines, corresponding to right vertical axis); (c) magnetic field in x and y direction; (d) the variation of the magnetic field (relative to the initial values); (e) the x component of perpendicular current density variation driven by the solar wind ions; (f) the x component of perpendicular current density variation (from the sum of foreshock ion and solar wind ion current and from $\nabla \times B$); (h) the y component of perpendicular current density variation driven by the solar wind ions; (i) the y component of perpendicular current density variation driven by the foreshock ions; (j) the y component of total perpendicular current density variation. Blue and red indicate ions from Region 1 and Region 2, respectively. The vertical dashed line indicates the TD position.

Figure 3 shows a vertical slice at $x=700 \ \lambda_i$ at the Bottom TD at the same time as Figure 2b. Figure 3d shows that at the TD, there is negative dB_x and bipolar dB_y , which is responsible for the field strength depletion in the core. The negative dB_x is caused by the bipolar J_y (Figure 3j) and the bipolar dB_y is caused by the two negative J_x peaks (Figure 3g). To determine the origin of current density profiles, we separate ion populations into solar wind ions and foreshock ions based on sunward/anti-sunward V_x and whether they are from Region 1 (blue) or Region 2 (red). (Sunward/anti-sunward refers to negative/positive x direction given the context of HFAs in the dayside foreshock.)

In the ion densities, the foreshock ions originating in Region 1 (dashed blue line) cross the TD centered at z=150 λ_i and travel up to z=200 λ_i in Region 2. Similarly, the foreshock ions originating in Region 2 (dashed red line) cross the TD and reach nearly z=100 λ_i in Region 1. The TD crossings of foreshock ions are influenced by their periodic velocity oscillation (possibly due to the foreshock ULF waves). For example, when foreshock ions initially gyrate towards the -y direction (out-of-plane direction), the foreshock ions from Region 1 (Region 2) cross the TD deeper (shallower) as their initial guiding centers are at larger +z positions than their initial positions.

225

226

227

228

229

230

231

232

233

234

235

236

237

238

239

240

241

242

243

244

245

246

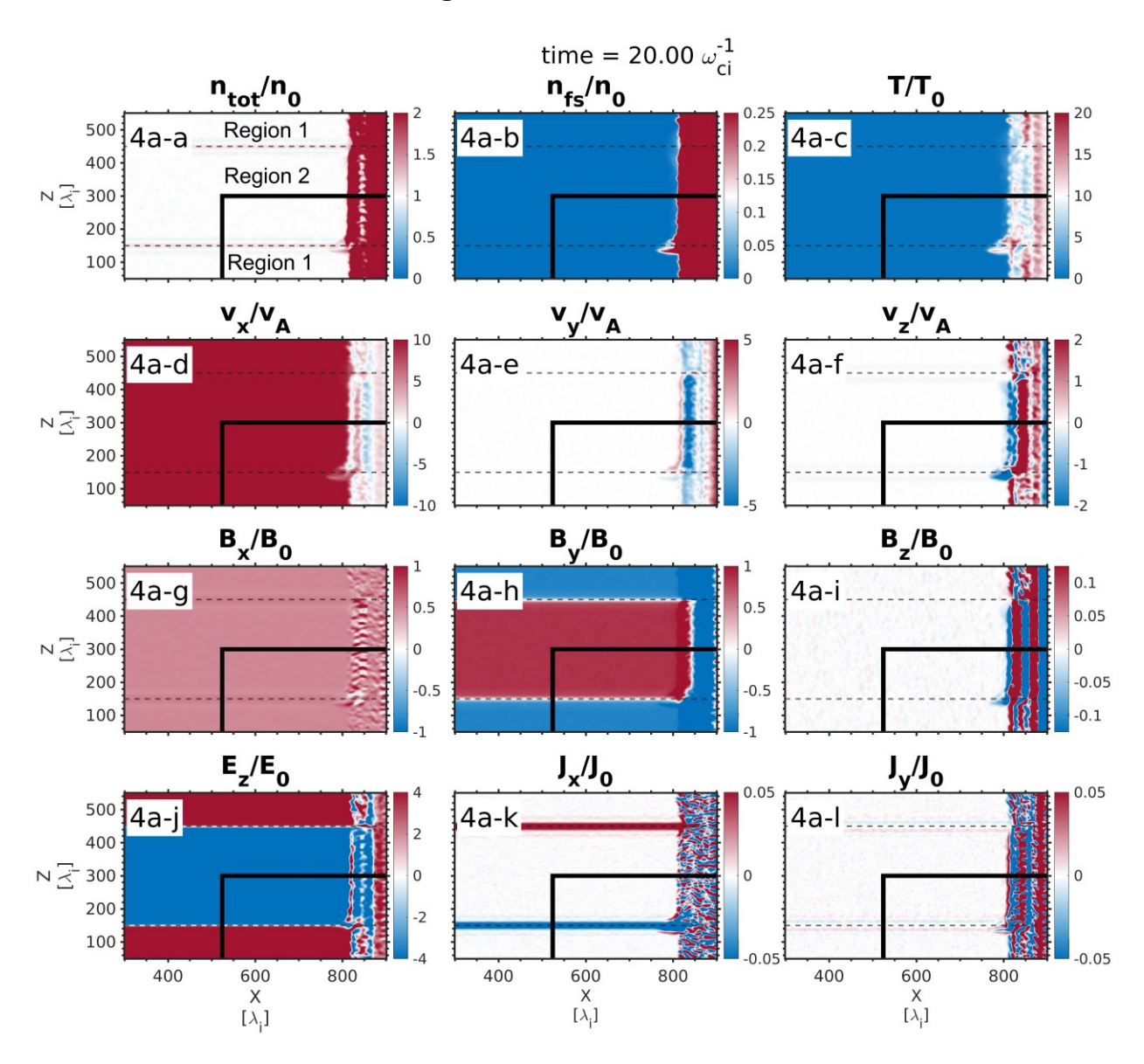
247

For each ion species (solar wind ions, foreshock ions, from Region 1, and from Region 2), we show their x component and y component of the perpendicular current densities in Figure 3. We see that the foreshock ions from above the TD (z>150, solid red line) generate a strong -J_v peak below the TD, and the foreshock ions from below the TD (z<150, solid blue line) generate a strong +J_v peak above the TD (Figure 3i). Such current direction is consistent with the partial gyration direction of foreshock ions as they gyrate across the TD. In contrast, the solar wind ions do not cross the TD and locally drive a current opposite to the foreshock ion-driven current (Figure 3h). Summing the solar wind and foreshock ion contributions from both Regions, we see that the net current has a significant -Jy peak below the TD and a significant +Jy peak above the TD (Figure 3j). As the net current direction is in the same sense as the foreshock ion-driven current, the foreshock ion-driven current tends to drive the field evolution and transfer energy to the magnetic field, whereas the solar wind ions resist it and gain energy as they move together with the field lines, consistent with models by An et al. (2020) and Liu et al. (2020b). This bipolar current profile is responsible for the B_x depletion within the HFA core and the enhancements on either side of the TD (Figures 3c and 3d). When the foreshock ions from region 1 (region 2) gyrate across the TD

in +y (-y) direction, they drive the current in the +x direction on the initial side and -x direction on the other side (Figure 3f) due to their initial gyrovelocity projected to the local perpendicular direction with $+B_x$ and $\mp B_y$ ($\pm B_y$). (Although initial field-aligned velocity should contribute a sunward -x component, it likely plays a minor role here.) Such J_x profile causes the B_y magnitude depletion in the core and enhancements at the two boundaries. Altogether, the net effect of the foreshock-driven current profile is the decrease of the field strength at the TD and the increase on two sides.

The gyrophase of foreshock ions also affects the current density profile. When the foreshock ions initially gyrate towards the -y direction, the current density in Region 2 (Region 1) becomes stronger (weaker). This causes meandering shape of the current density profile during early formation (see Movie M1 in the supporting information). No matter what gyrophase of foreshock ions is, the decreased field strength in the core region always favors more foreshock ions to cross the TD and be trapped within it, leading to further growth of the structure.

In this run, the cone angle is symmetrical on two sides of the TD leading to similar foreshock ion conditions. We also test the case with cone angle changing from -15° to 40° shown in Figures S1 and S2 in the supporting information. The formation process and the current geometry are essentially the same as Case 1 except with slight asymmetry.



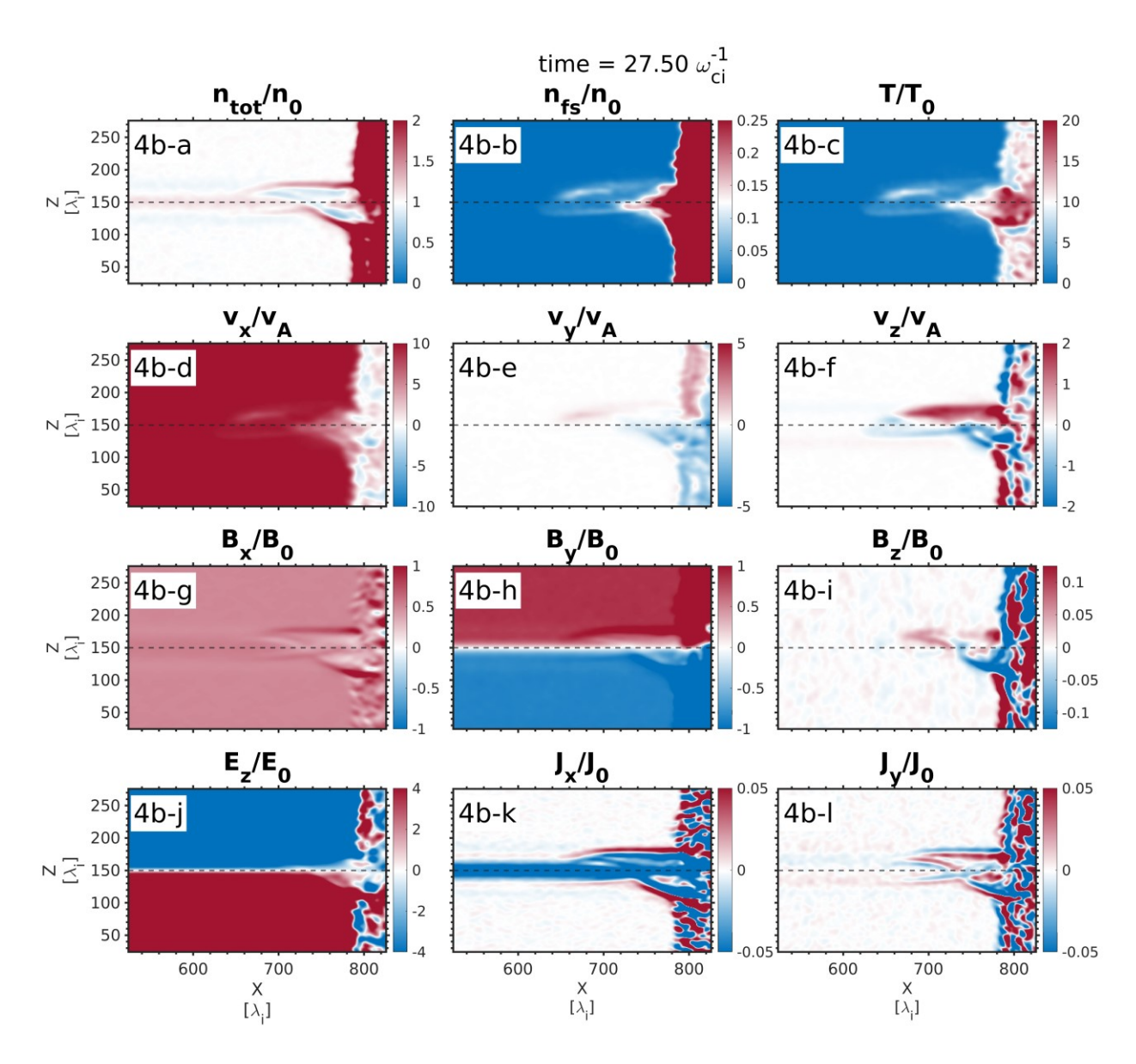


Figure 4 – 2-D plots for Case 2 with cone angle changing from -60° to +60° and back to -60°, in the same format as Figure 2. Note that in Figure 4a-h, there is a vertical layer at $x\sim800-850$ λ_i that convects downstream. It is for the two TDs to intersect a uniform shock through setting up uniform cone angle right side of the layer by varying B_y .

Next, we present a case where the cone angle changes from -60° to $+60^{\circ}$ and back to -60° . This makes both sides of the TDs have quasi-perpendicular shocks where the foreshock ions hardly

travel upstream away from the shock surface (Figure 4a-b). Because there are no clear background foreshock ions, we would not expect the formation of a foreshock transient. However, our simulation shows otherwise. This can be seen at the Bottom TD, where there is a density depletion bounded by compressional boundaries earlier in the simulation (Figure 4a-a), which expands further upstream and along the planar shock surface to be a larger structure later in the simulation (Figure 4b-a). It eventually grows into a very large structure with significant density and field strength depletion (see Movie M2 in the supporting information). The ion density panels reveal a concentration of foreshock ions (or backstreaming ions in Figure 4b-b) within the heated core (Figure 4b-c). The core also exhibits a velocity deflection/deceleration (Figure 4b-d) and magnetic field depletion (Figure 4b-g). The Top TD, on the other hand, does not form any structures. We focus on the Bottom TD, where an HFA is formed without background foreshock ions.

Figure 5 shows the 1-D profile at $x=700 \lambda_i$ where the structure is more along the TD surface. The formation is likely related to the initial geometry of the TD. While the cone angle, or θ_{Bn} , changes from -60° to +60°, there exists a spatial region within the TD that possesses a 0° cone angle, or θ_{Bn} , i.e., the magnetic field is exactly parallel to the planar shock normal. This can be seen early on in Figure 4a-h by the white region in the magnitudes of B_y, designating a 0° cone angle. Thus, because of the parallel shock geometry and the area around it, sheath ions can easily travel upstream along the center of the TD at the connection point of the TD and the planar shock. These backstreaming ions can then create a current (Figures 5f, g, i, j) with profiles similar to Case 1 (double -J_x peaks and bipolar J_y) that decreases the field strength inside the TD (Figures 5d) and widens this parallel shock region. This allows more ions from the sheath to travel into the TD or the proto core of the structure. This runaway process will cause the core to expand outward from the center of the TD continuously and thus form a significant HFA.

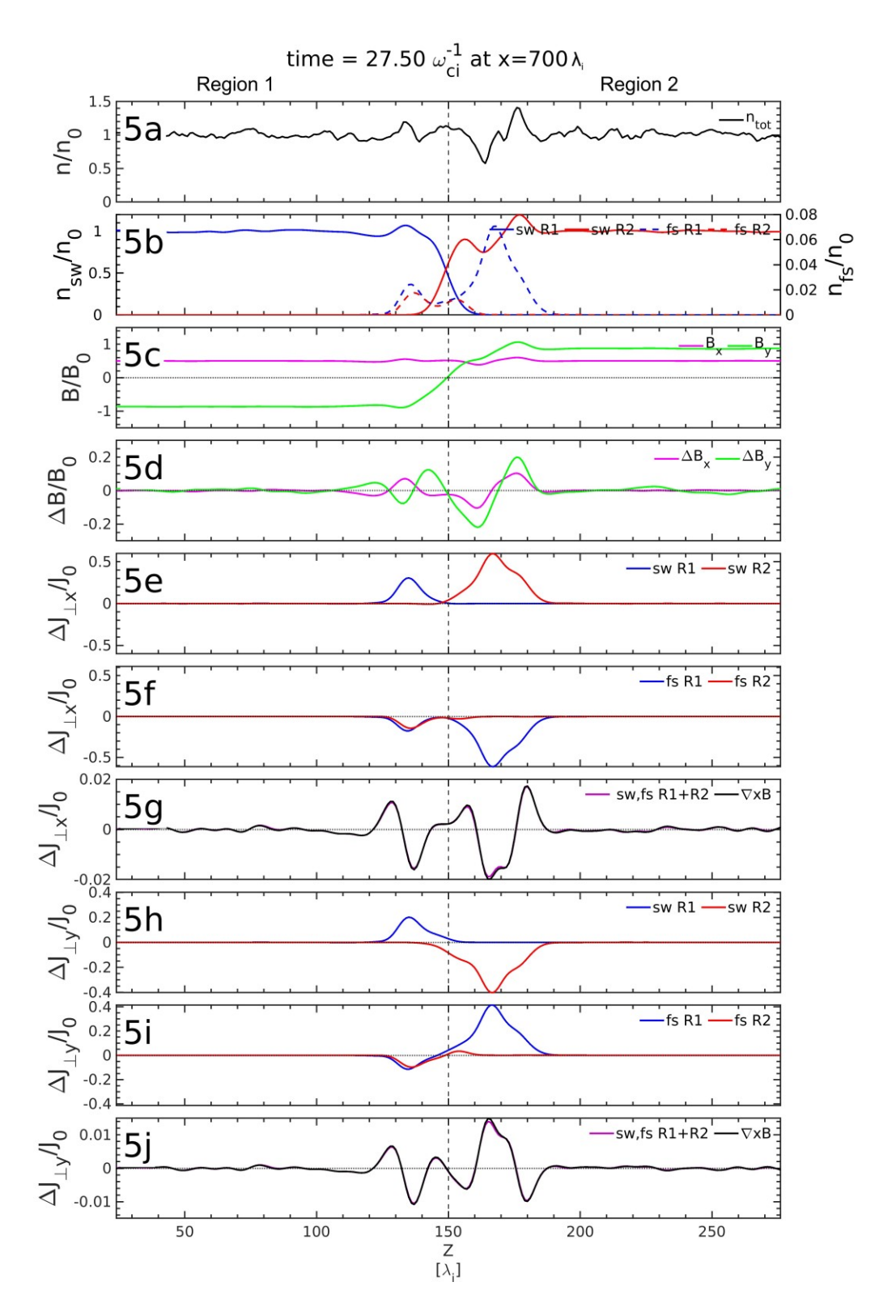


Figure 5 – 1-D profile for Case 2 at $x=700 \ \lambda_i$ at the same time as Figure 4b, in the same format as Figure 3.

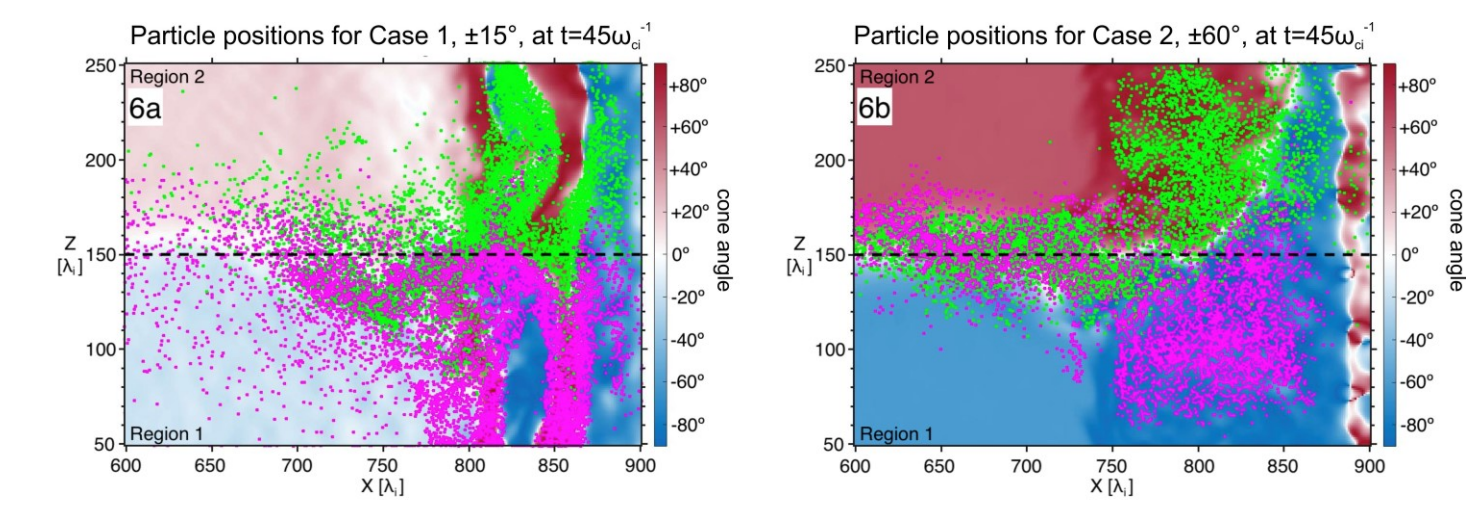


Figure 6 –Particle tracing for Case 1 and Case 2 at the Bottom TD. The formation of the HFA occurs in both cases. However, the formation of the HFA in Case 1 is facilitated by the ions from the background foreshock. In contrast, the formation of the HFA in Case 2 is facilitated by the leakage of ions directly from the sheath. The magenta-colored particles represent ions that originated below the TD centered at $z=150~\lambda_i$, and the green-colored particles represent ions that originated above the TD.

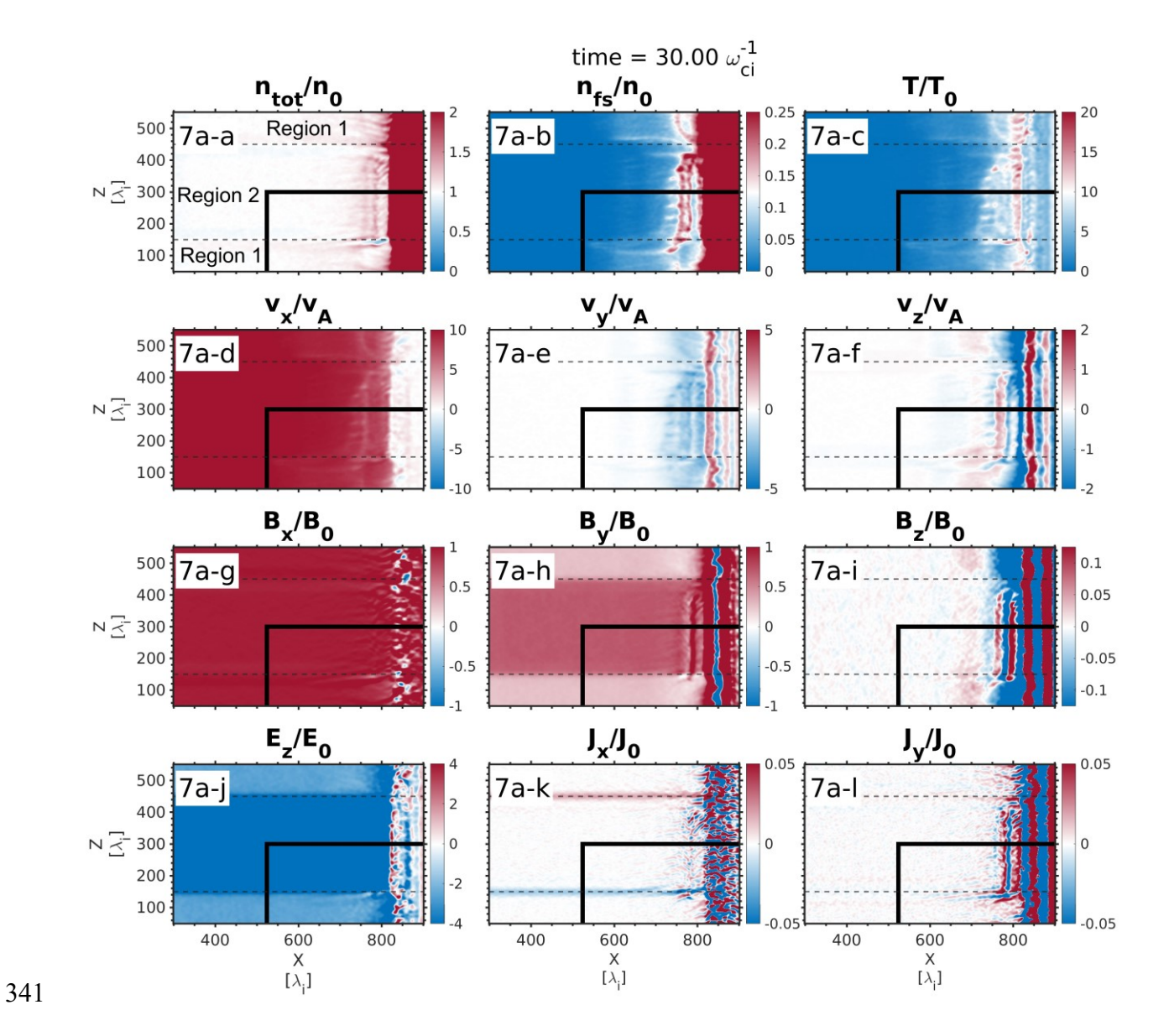
To further examine the origin of the backstreaming ions in the core, we trace the ions within a certain spatial region at $t=45\omega_{ci}^{-1}$ within the HFA core backward. Figure 6 shows a snapshot of the particle tracing results compared to Case 1 with a 15° cone angle. Movies of the ion tracing results can be found in the supporting information (Movies M3 and M4). Based on whether the ions directly enter the core from the sheath region or first reach the upstream background foreshock region and then enter the core, we can categorize their origin as either leaked ions or background foreshock ions, respectively. To categorize them, we track the ion macroparticles that cross the planar shock and enter the sheath. If these particles later turn back and leave the shock, we note

their positions relative to the structure when they leave the shock surface. We classify the ion macroparticles as being "background" or "leak" if their z position is outside or inside of the structure when they leave the shock surface, respectively.

Tracking the ion macroparticles as they leave the shock, we find that for the cone angle of 15° in Case 1, the background foreshock ions account for 90% of the initial formation of the HFA. For the cone angle of 60° in Case 2, the leakage of ions into the TD accounts for more than 95% of the initial formation of the HFA. Furthermore, we find that in Case 1, there is a higher percentage of leaked ions within the core of the HFA than background ions at later times when the HFA structure is more mature and wider. In all, we find that in Case 1, the quasi-parallel case, the background foreshock ions are the major reason for the early formation of the HFA, whereas, in the quasi-perpendicular case, the leaked ions jumpstart the HFA formation process.

3.3. Case 3 – +15° to +45° Cone Angle

Next, we present a case where the cone angle has the same sign on two sides. Because of the different cone angle magnitudes, the foreshock ions show different properties on two sides. In this setup, the z component of the electric field, normal to the TDs, is directed towards the Bottom TD from above in Region 2 and towards the Top TD from above in Region 1 (Figure 7a-j). In other words, there is only one side of the TD which has an electric field pointing towards it. At the Bottom TD, an HFA forms. It is recognized by the development of a depleted, hot core region with flow deflection/deceleration bounded by two compressional boundaries (Figures 7b-a, 7b-c, 7b-d, 7b-g). At the Top TD, a compressional boundary with enhanced density and field strength forms, which is examined in the accompanying paper (Vu et al., submitted to JGR). Although both TDs have electric fields pointing towards them on one side, only one TD forms an HFA. Comparison in their formation differences is discussed in the accompanying paper.



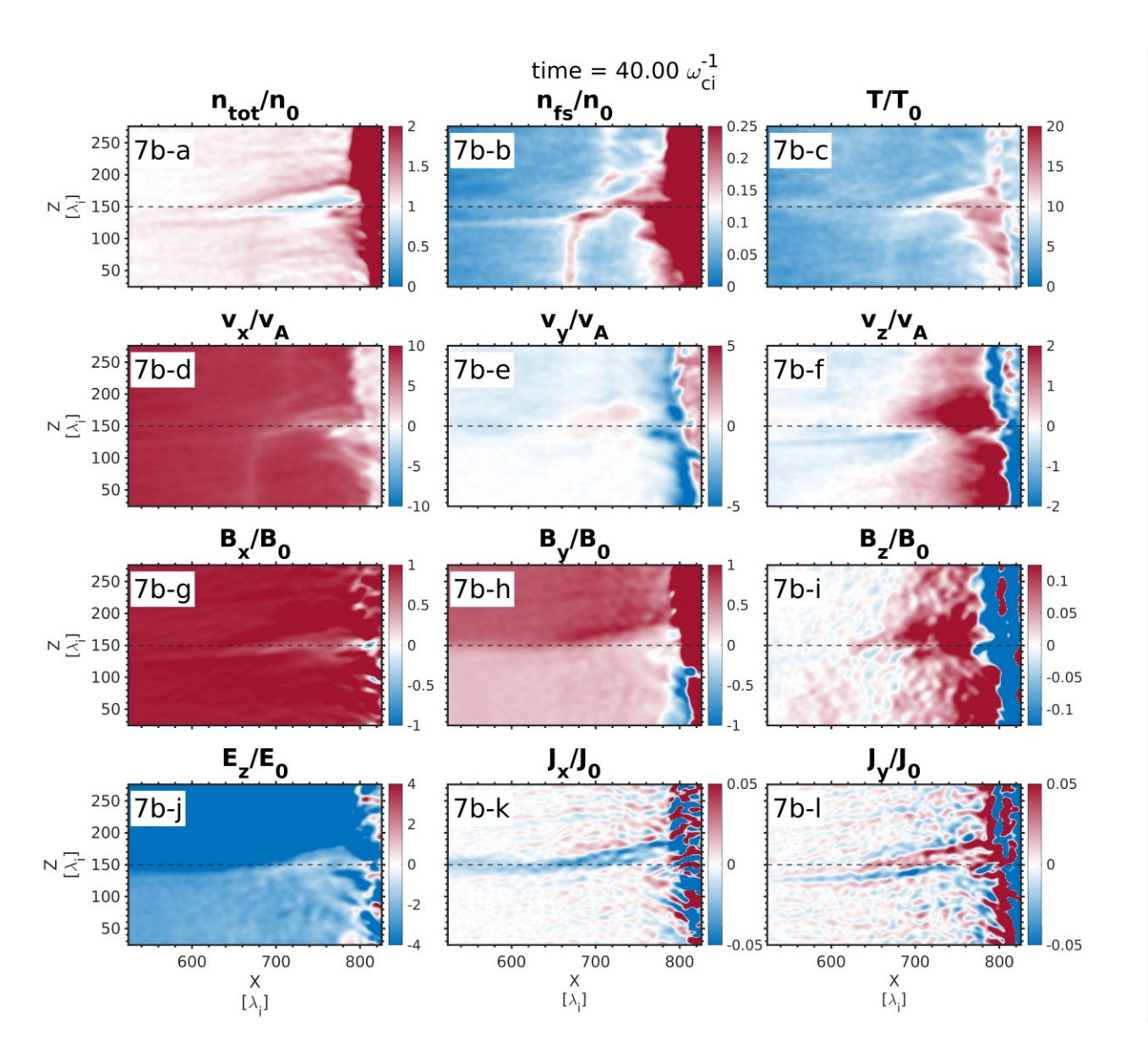


Figure 7 – 2-D plots for Case 3 with cone angle changing from $+15^{\circ}$ to $+45^{\circ}$ and back to $+15^{\circ}$, in the same format as Figure 2.

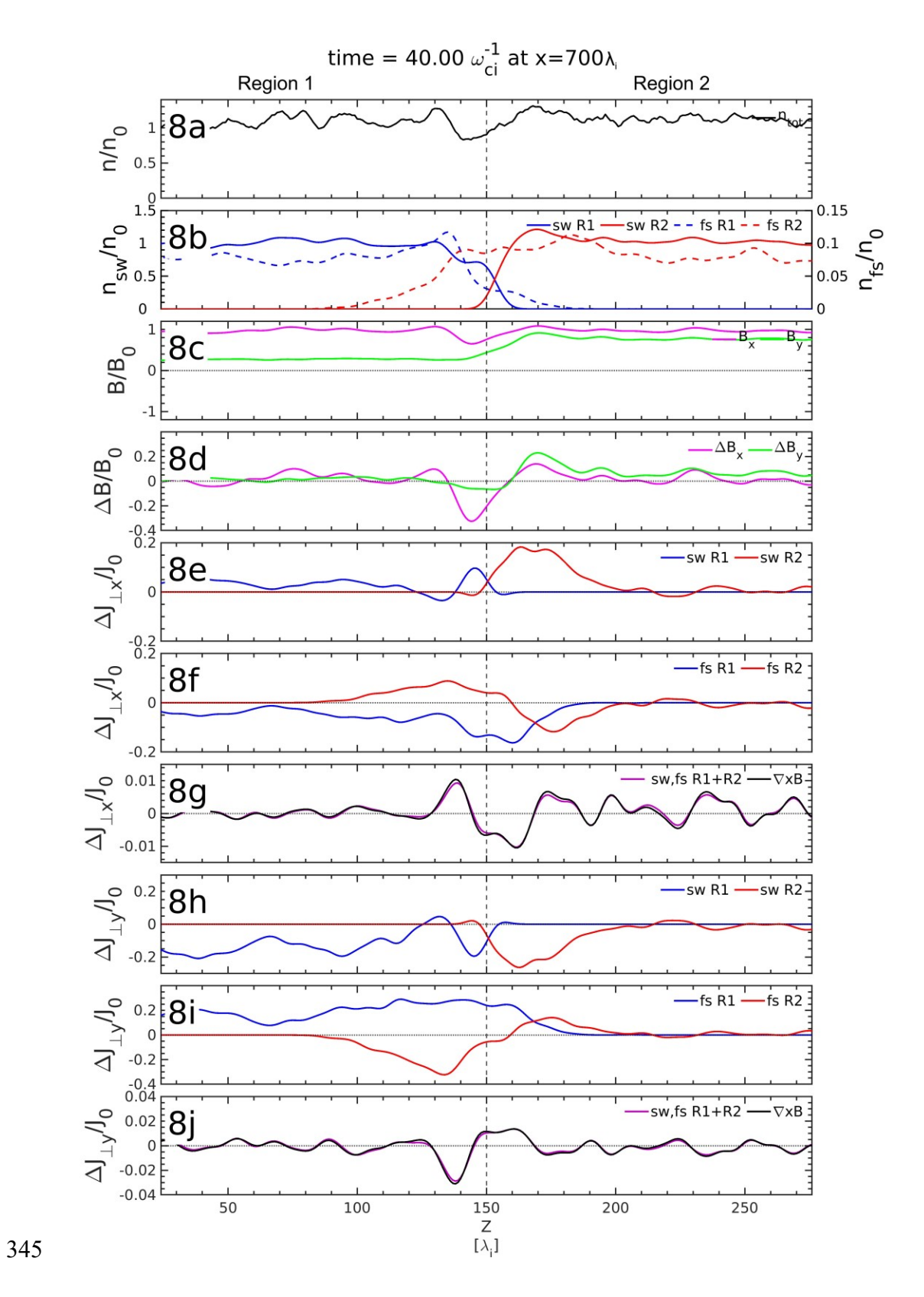


Figure 8 – 1-D profile for Case 3 at $x=700 \lambda_i$ at the same time as Figure 7b, in the same format as Figure 3.

Figure 8 shows the 1-D cut through our simulation of an HFA at the same time as Figure 7b at x=700 λ_i . Figure 8b shows that although foreshock ions from Region 2 (above the TD, dashed red line) have similar background densities to those from Region 1 (below the TD, dashed blue line), the foreshock ions from Region 2 cross the TD (at z=150 λ_i) deeper into Region 1 (about z=100 λ_i) than the foreshock ions from Region 1 into Region 2 (about z=170 λ_i). This difference persists unlike Case 1, likely because the strong +B_y in Region 2 causes sunward ions (-V_x) to have motion preference towards -z direction.

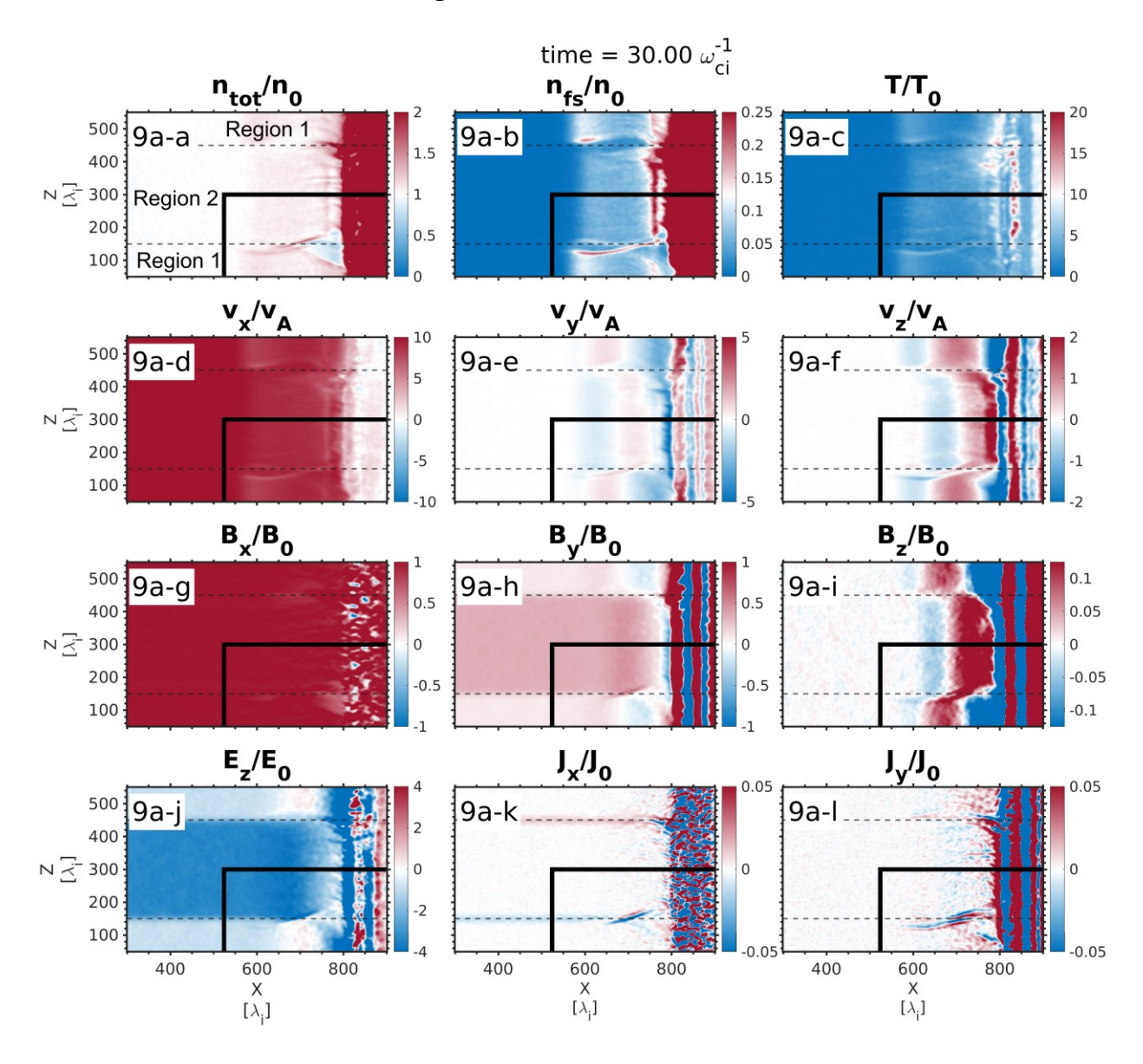
By decomposing the current densities by solar wind or foreshock ion species, we see that the foreshock ions originating in Region 2 (red; above the TD at $z>150 \lambda_i$) generate a +J_x and -J_y mostly in Region 1 below the TD, and the foreshock ions originating in Region 1 (blue; below the TD at $z<150 \lambda_i$) generate a -J_x and +J_y slightly across the TD to Region 2 (Figures 8f and 8i). These two currents are mostly due to the initial gyration of foreshock ions from the two sides. If there is no TD and the foreshock ion properties are uniform, these two currents will cancel each other. Here, due to the field change across the TD and different foreshock ion properties in the two regions, the two currents peak at different locations resulting in a net bipolar perpendicular current in the x and y components. The solar wind ions have currents in opposite directions but cannot suppress or reverse this bipolar trend. The bipolar J_y decreases B_x in the core region while the bipolar J_x decreases B_y (Figure 8d). Such field variations create the early field profile of the HFA.

Because foreshock ions are typically supward, they usually exhibit a supward current (I_x <0)

Because foreshock ions are typically sunward, they usually exhibit a sunward current ($J_x < 0$) (such as in Case 1), but in this case foreshock ions from Region 2 exhibit an anti-sunward current

 $(J_x>0)$. When the foreshock ions in Region 2 gyrate across the TD (in -z direction), their local perpendicular velocity has a -y component (Figure 8i) due to $+B_x$ (Figure 8c). Because of $+B_y$, the local perpendicular velocity needs to have +x component (Figure 8f). In this simulation case, the initial gyrovelocity contributes a larger anti-sunward component than the initial field-aligned velocity that typically contributes a sunward component. Whether the foreshock ion-driven current is sunward or anti-sunward leads to different implications of the convection electric field direction, which is discussed in Section 4.





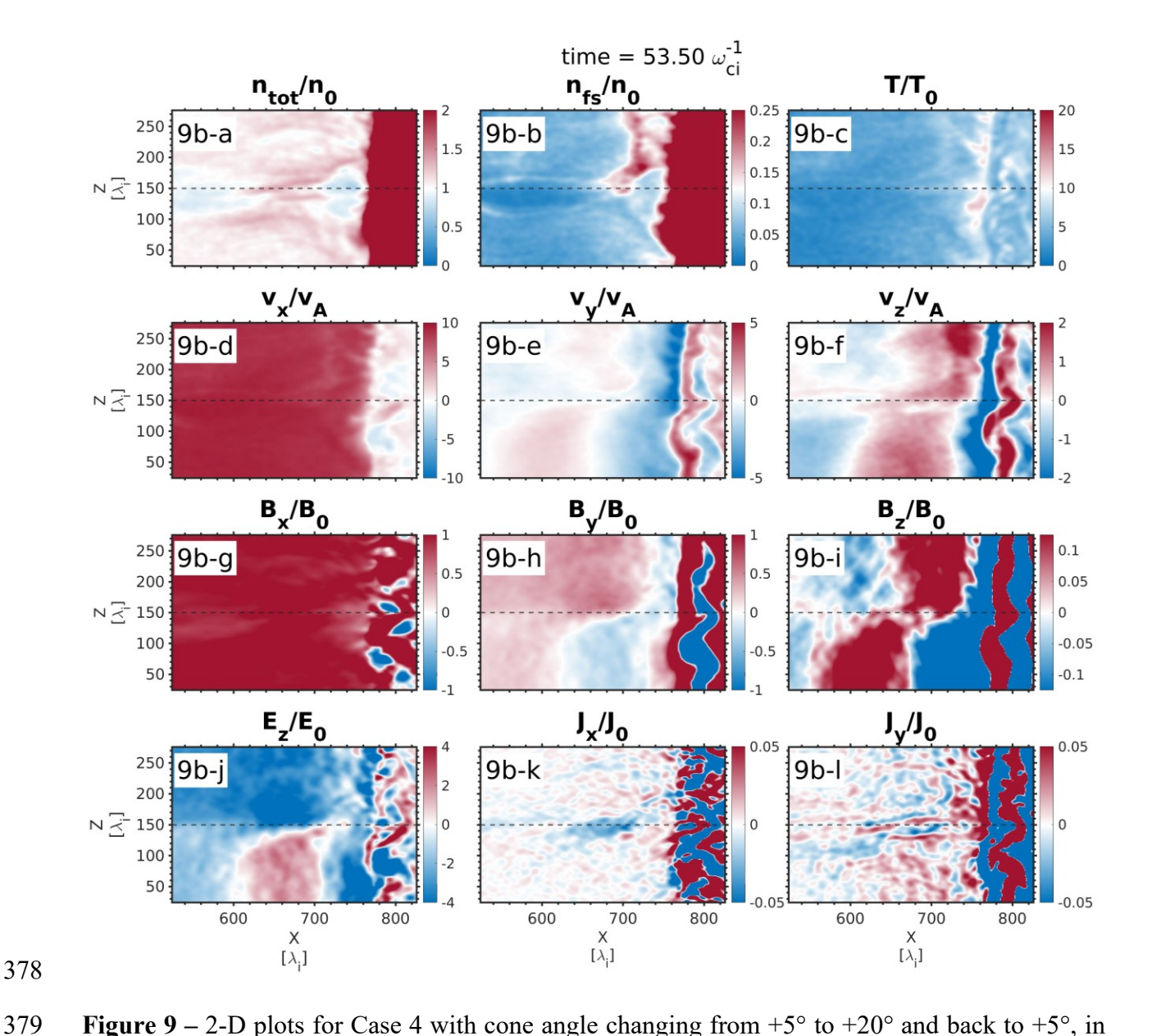


Figure 9 – 2-D plots for Case 4 with cone angle changing from $+5^{\circ}$ to $+20^{\circ}$ and back to $+5^{\circ}$, in the same format as Figure 2.

In this case, the cone angle in Region 1 is $+5^{\circ}$, and in Region 2 is $+20^{\circ}$. Because of the very small cone angle in Region 1, there are strong foreshock ULF waves with amplitude dB_y larger than the small background B_y . As a result, the foreshock ULF waves locally reverse the direction of B_y and E_z even during the very early time (see local blue B_y and red E_z in Figures 9a-h, 9b-h

and 9a-j, 9b-j). Such variations can locally modify and ultimately control how foreshock ions interact with TDs. Without the field reversal, the formation process is similar to Case 3. Below we focus on the region where B_v is reversed.

Figure 10 shows the 1-D profile cut through the region where B_y is reversed to be negative in Region 1 (Figure 10c), causing the convection electric field to point towards the Bottom TD on both sides. When the foreshock ions from Region 1 (Region 2) cross the TD, their initial gyrovelocity contributes to +y component (-y component) to the perpendicular velocity (Figure 10i). Because of the reversed B_y, the contribution to the x component of perpendicular velocity reverses from positive to negative (negative to positive) (Figure 10f). Thus, the net current profile is a bipolar J_y (Figure 10j) and two -J_x peaks (Figure 10g). Such current configuration is consistent with Case 1 with background B_y set to be reversed.

Possibly because a bipolar J_x configuration like in Case 3 is more efficient in decreasing B_y magnitude than the two $-J_x$ peaks in Case 1 (their B_y variation weakens each other between them), the formed HFA core is narrower (Figure 9b-a at $x\sim600-700~\lambda_i$) at the ULF wave phases where B_y is reversed resulting in periodic variation in HFA shape along the x direction. This periodic variation propagates together with the ULF waves (see Movie M6 in the supporting information). In summary, due to their long wavelengths/periods, foreshock ULF waves with large amplitude can significantly modify the local background field seen by the foreshock ions, which periodically affects how foreshock ions interact with a discontinuity and the formed structure. This process could interrupt and possibly weaken the growth of the HFA.

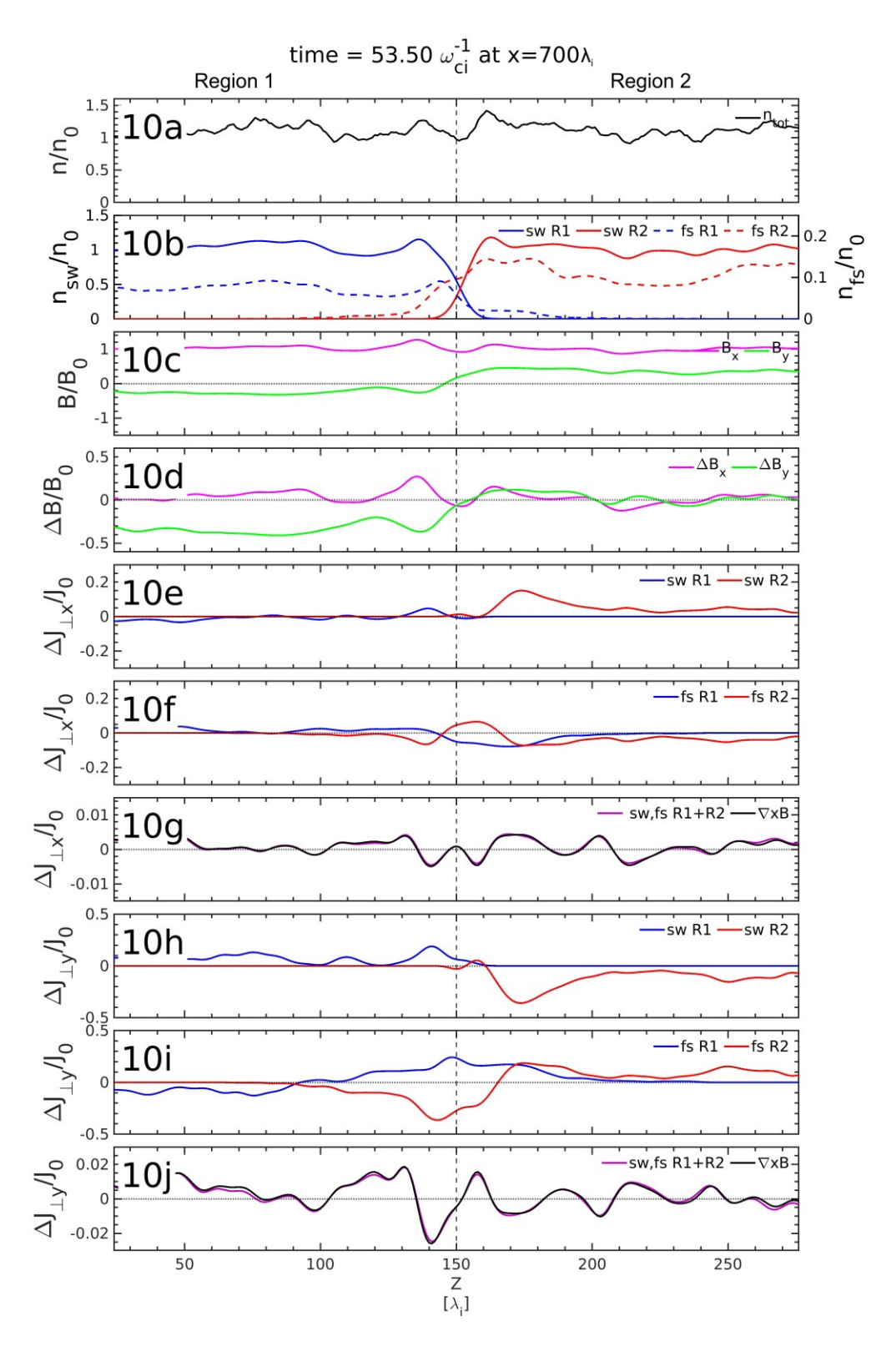


Figure 10 – 1-D profile for Case 4 at $x=700 \ \lambda_i$ at the same time as Figure 9b, in the same format as Figure 3.

4. Discussion

Here, we summarize the formation conditions of HFAs. We also discuss the role of convection electric field direction as an indicator of HFA formation. When foreshock ions cross a TD to the other side (e.g., from Region 1 to Region 2), their velocity encounters an abrupt change of magnetic field direction, causing partial gyration in the local field and thus a current J. If J decreases the field strength at the TD, more foreshock ions can cross the TD and contribute to J favoring the formation and growth of an HFA, which depends on the J direction relative to the magnetic field geometry around the TD, as discussed below.

- (1) When the foreshock ion velocity perpendicular to the local field is mainly contributed by the initial sunward velocity, J is sunward (e.g., Figures 3f and 5f in Cases 1 and 2). Thus, $J \times B$ direction is in the same sense as $-V_{sw} \times B$ direction, where V_{sw} is the solar wind velocity in the simulation (or spacecraft) rest frame. Because J decreases field strength on the side pointed by $J \times B$ direction, the convection electric field direction becomes an indicator of HFA formation. For example, when the electric field points towards the TD in Region 2 and away from the TD in Region 1, the foreshock ions in Region 1 (Region 2) cross the TD and generate J in Region 2 (Region 1) that decreases (increases) field strength at the TD, favoring (not favoring) the formation of an HFA. Therefore, whether an HFA forms depends on whether the foreshock ions in Region 1 (Region 2) dominate the current. Similarly, when the electric field points towards the TD on both sides, the foreshock ions from both sides cross the TD and generate J that favors the formation of an HFA (e.g., Cases 1 and 2).
- (2) When the foreshock ion velocity perpendicular to the local field is mainly contributed by the initial gyrovelocity, the convection electric field direction can be an indicator of whether this perpendicular velocity is sunward. When the foreshock ions cross a TD along the normal direction

 \hat{n} , the x direction of Lorentz force, $(\hat{V}_n \times \hat{B}) \cdot \hat{x} = (-\hat{x} \times \hat{B}) \cdot \hat{V}_n$, indicates the gyration tendency along x (where +x is anti-sunward in the simulation coordinate). If we define n as positive towards the TD, $(-\hat{x} \times \hat{B}) \cdot \hat{V}_n$ has the same (opposite) sign as $(-\hat{V}_{sw} \times \hat{B}) \cdot \hat{n} \sim (-\hat{x} \times \hat{B}) \cdot \hat{n}$ before (after) the foreshock ions cross the TD center. For example, when the electric field points towards the TD in Region 2 and away from the TD in Region 1, the foreshock ions from Region 1 (Region 2) tend to gyrate in the sunward (anti-sunward) direction around the TD. Thus, though the electric field points away from the TD in Region 1, the foreshock ions from Region 2 have $J \times B$ directed towards the TD in Region 1, whereas the foreshock ions from Region 1 have $J \times B$ directed towards the TD in Region 2 - same as the convection electric field direction. So, both currents from Region 1 and Region 2 tend to decrease the field strength at the TD (e.g., Figures 8f and 8i in Case 3).

If the electric field points towards (away from) the TD on both sides, the Lorentz force direction of foreshock ion gyrovelocity is anti-sunward (sunward) before crossing the TD center and sunward (anti-sunward) after crossing the TD center. In this case, before the TD center, the generated J tends to increase (decrease) field strength at the TD; after the TD center, J tends to decrease (increase) field strength at the TD. Thus, whether an HFA can form depends on which part of J is stronger (before or after the TD center). Because the calculation of J requires subtracting the anti-sunward solar wind electron velocity, the sunward part of J is more likely to be stronger than the anti-sunward part of J. Thus, when the electric field points towards the TD on both sides, the sunward part of J after the TD dominates (e.g., Figure 3f in Case 1), which favors the formation of an HFA.

The convection electric field direction is frame dependent. For example, in the solar wind rest frame, the electric field is zero, so the physical meaning of electric field direction becomes unclear.

Because the solar wind speed is always anti-sunward, the convection electric field direction is an indicator of magnetic field geometry and how the foreshock ions interact with it. Whether the convection electric field points towards a TD is neither a sufficient nor a necessary condition for the HFA formation (as observed by Wang et al. (2013) and Liu et al. (2023b)) because it also relies on the foreshock ion properties, like whether the gyrovelocity or the field-aligned velocity dominates the current direction, whether the foreshock ions can cross the TD, and which side of foreshock ions provides stronger current. Nevertheless, the convection electric field direction is still a good indicator because when the convection electric field points away from the TD, more extreme requirements from foreshock ion properties are needed to generate an HFA. However, to accurately predict HFAs and forecast their geoeffectiveness efficiently, a more rigorous model, including both field geometry and foreshock ion properties, is required.

In the above discussion, we only considered a stable background field. However, as shown in Case 4, foreshock ULF waves can have amplitudes large enough to modulate the background field and, thus, the foreshock ion current geometry. Without a stable environment for the structure to grow, the formed HFA could be relatively weak. Although strong foreshock ULF waves are likely unfavorable for HFAs, they are expected to drive more spontaneous foreshock transients, like foreshock cavitons, spontaneous HFAs, and SLAMS (see review by Zhang et al. (2022) and references therein).

In this study, the role of various magnetic field geometries in HFA formation is examined. Many other parameters still need to be further investigated. (1) Statistical studies (e.g., Schwartz et al., 2000; Liu et al., 2021) showed that when TD planes are more along the bow shock normal, HFAs more likely occur. Hybrid simulations by Giacalone and Burgess (2010) also showed that HFAs are more significant when TD planes are more along the shock normal. One explanation is

that such a TD geometry favors slow transit speed along the shock surface allowing sufficient time to interact with the foreshock ions. This, however, cannot explain the situation in the midtail foreshock where the bow shock surface is rather tilted (at GSE-X ~-30 - -50 R_E). Thus, the exact role of TD inclination is still not fully clear. (2) A statistical study by Zhao et al. (2017) showed that moderately thin TDs favor the formation of HFAs. Foreshock ion-driven current model by Liu et al. (2023b) provided a quantitative relationship between the TD thickness and current strength. Although hybrid simulations by Vu et al. (2022) demonstrated how different TD thickness affects the current geometry, the parameter dependence on the TD thickness remains to be tested. (3) In the models and local simulations, a planar shock is used whereas the bow shock is curved. To role of shock curvature should be included, which is especially important for HFAs at different planetary bow shocks. For example, a curved bow shock can cause spatial variations of foreshock ion properties, and there is a finite ion foreshock spatial scale that limits the growth of HFAs. Additionally, HFAs have a more complicated 3-D shape at a bow shock than at a planar shock.

Below we discuss the limitations of our 2-D simulation setup. (1) The field-aligned waves and structures at the shock ramp may not be properly modeled in 2-D simulations. As a result, the downstream ions could not be fully isotropized causing gyromotion to dominate (e.g., see periodic V_y and V_z downstream of the shock in Figures 2a-e and 2a-f). Therefore, the role of backstreaming gyrating ions could be over-emphasized. If there are more backstreaming field-aligned ions, the current will be more dominated by the sunward component. Additionally, the strong anisotropy may also drive more field fluctuations than reality (e.g., through cyclotron resonance with gyrating ions). (2) The foreshock ULF waves have not fully developed before the formation of HFAs starts, leading to unrealistic foreshock environment. As inferred from Case 4, if the foreshock ULF waves

have fully developed, the formation of HFAs can be interrupted, weakened or even suppressed. Statistical study by Liu et al. (2022) shows that a very small θ_{Bn} is not a favorable condition for HFAs possibly due to the strong wave activities. In the future, more realistic setup such as 3-D global hybrid simulations could be conducted to fully examine the HFA formation processes.

In Case 2, we see the HFA formed in the quasi-perpendicular region can become more significant than Case 1 in the quasi-parallel region (see Movies M1 and M2 in the supporting information). One possible reason is the very large shear angle that favors large velocity projection and thus current strength (Vu et al., 2023). This is consistent with statistical studies (e.g., Schwartz et al., 2000; Zhao et al., 2017) that HFAs more likely occur at large shear angles. Another reason is that expansion into the pristine solar wind is easier than into the hot foreshock. Additionally, the sheath leakage could be over emphasized due to the simulation setup. HFAs embedded in the quasi-perpendicular region is only occasionally observed (e.g., Zhang et al., 2010; Wang et al., 2013). It is probably because to have small θ_{Bn} within a TD, the TD surface should be roughly along the shock normal. As the TD moves along the bow shock surface that is curved, the formation of such HFAs is rather limited.

5. Conclusions

Using local hybrid simulations, we examine the formation of HFAs under various magnetic field geometries across TDs embedded in the quasi-parallel region. When foreshock ions cross the TD to the other side, they perform a partial gyration where a portion of their initial motion gets projected into the local perpendicular direction. This generates a perpendicular current that changes the magnetic field around the TD. The convection electric field direction works as a proxy of whether the generated current increases or decreases the field strength at the TD. In our setups, the foreshock ions from one side of the TD cross the TD and account for the HFA compressional

boundary formation on the other side of the TD. Foreshock ions from both sides contribute to forming a low-field strength core. There are also situations where the foreshock ions cannot cross the TD and the foreshock ions from two sides compete each other, examined in the accompanying paper (Vu et al., submitted to JGR).

When the TD is embedded in the quasi-perpendicular region, a quasi-parallel region within the TD could occur filled with backstreaming ions. Under favorable magnetic field geometry, such ions can generate current that decreases field strength within the TD and widens the quasi-parallel region leading to more backstreaming ions. Eventually an HFA forms without background foreshock ions on two sides.

When the TD is embedded in the quasi-parallel region with small θ_{Bn} , there are foreshock ULF waves with large amplitudes. With sunward shock normal and nearly radial IMF, the large wave fluctuations in the transverse direction can easily modulate the background field geometry and the convection electric field direction. The wave periods in the shock rest frame are long enough for the foreshock ions to respond to such periodic background field variation. As a result, the foreshock ULF waves can periodically modulate and possibly weaken the HFA formation.

In the previous models (Liu et al., 2023a, 2023b, 2023c), foreshock ions from only one side of TDs were considered for simplicity. Based on this study, these models can now be generalized to the situation when there are foreshock ions from both sides. For example, during the early formation stage, the current density profile could be the superposition of foreshock ion-driven current from two sides, determined by the initial foreshock ion properties on each side (e.g., gyrophase, density, etc.). During the late expansion stage, in addition to the energy transfer from the background foreshock ions on two sides, it is notable that the local magnetosheath leakage might also contribute to the formation and evolution process depending on the magnetic field

geometry within HFAs relative to the bow shock. More modeling efforts and comparisons with simulations and observations are needed to advance our understanding in this area.

Acknowledgements

549

554

557

T. Z. L. and A. V. acknowledge NSF award AGS-1941012/2210319, NASA grant 80NSSC22K0791 and NASA grant 80NSSC23K0086. H. Z. is partially supported by NSF AGS-1352669 and NASA grant 80NSSC18K1376. We acknowledge support by the NASA THEMIS contract NAS5-02099.

Open Research

The simulation data output that was used for the figures and analysis in this study is available at (Vu, 2023a, 2023b).

References

- An, X., Liu, T. Z., Bortnik, J., Osmane, A., & Angelopoulos, V. (2020). Formation of Foreshock
- Transients and Associated Secondary Shocks. *The Astrophysical Journal*, 901(1).
- 560 https://doi.org/10.3847/1538-4357/abaf03
- Archer, M. O., Turner, D. L., Eastwood, J. P., Horbury, T. S., & Schwartz, S. J. (2014). The role
- of pressure gradients in driving sunward magnetosheath flows and magnetopause motion.
- Journal of Geophysical Research: Space Physics, 119(10), 8117–8125.
- 564 https://doi.org/10.1002/2014JA020342
- Archer, M. ~O., Turner, D. ~L., Eastwood, J. ~P., Schwartz, S. ~J., & Horbury, T. ~S. (2015).
- Global impacts of a Foreshock Bubble: Magnetosheath, magnetopause and ground-based

- observations. *Planetary and Space Science*, 106, 56–66.
- 568 https://doi.org/10.1016/j.pss.2014.11.026
- 569 C. Chu, H. Zhang, D. Sibeck, A. Otto, Q. Zong, N. Omidi, J.P. McFadden, D. Fruehauff, V.
- Angelopoulos (2017). THEMIS satellite observations of hot flow anomalies at Earth's bow
- shock. Ann. Geophys. 35(3), 443–451. https://doi.org/10.5194/angeo-35-443-2017
- Delamere, P. A., Swift, D. W., & Stenbaek-Nielsen, H. C. (1999). A three-dimensional hybrid
- 573 code simulation of the December 1984 solar wind AMPTE release. *Geophysical Research*
- 574 Letters, 26(18), 2837–2840. https://doi.org/10.1029/1999GL900602
- Delamere, P. A. (2006). Hybrid code simulations of the solar wind interaction with Comet
- 576 19P/Borrelly. *Journal of Geophysical Research*, 111(A12).
- 577 https://doi.org/10.1029/2006JA011859
- Delamere, P. A. (2009). Hybrid code simulations of the solar wind interaction with Pluto.
- *Journal of Geophysical Research: Space Physics*, 114(3).
- 580 https://doi.org/10.1029/2008JA013756
- Eastwood, J. P., Lucek, E. A., Mazelle, C., Meziane, K., Narita, Y., Pickett, J., & Treumann, R.
- 582 A. (2005). The Foreshock. *Space Science Reviews*, 118(1), 41–94.
- 583 https://doi.org/10.1007/s11214-005-3824-3
- Facskó, G., Németh, Z., Erdos, G., Kis, A., & Dandouras, I. (2009). A global study of hot flow
- anomalies using Cluster multi-spacecraft measurements. *Annales Geophysicae*, 27(5),
- 586 2057–2076. https://doi.org/10.5194/angeo-27-2057-2009

587 Giacalone, J., and D. Burgess (2010), Interaction between inclined current sheets and the 588 heliospheric termination shock, Geophys. Res. Lett., 37, L19104, 589 doi:10.1029/2010GL044656. 590 Hartinger, M. D., Turner, D. L., Plaschke, F., Angelopoulos, V., & Singer, H. (2013). The role of 591 transient ion foreshock phenomena in driving Pc5 ULF wave activity. Journal of 592 Geophysical Research: Space Physics, 118(1), 299–312. 593 Jacobsen, K. S., Phan, T. D., Eastwood, J. P., Sibeck, D. G., Moen, J. I., Angelopoulos, V., 594 McFadden, J. P., Engebretson, M. J., Provan, G., Larson, D., & Fornaçon, K.-H. (2009). 595 THEMIS observations of extreme magnetopause motion caused by a hot flow anomaly. 596 Journal of Geophysical Research: Space Physics, 114(A8). 597 https://doi.org/10.1029/2008JA013873 598 Lin, Y. (1997). Generation of anomalous flows near the bow shock by its interaction with 599 interplanetary discontinuities. Journal of Geophysical Research: Space Physics, 102(A11). https://doi.org/10.1029/97JA01989 600 601 Lin, Y. (2002). Global hybrid simulation of hot flow anomalies near the bow shock and in the 602 magnetosheath. Planetary and Space Science, 50(5-6). https://doi.org/10.1016/S0032-603 0633(02)00037-5 604 Liu, Z., Turner, D. L., Angelopoulos, V., & Omidi, N. (2015). THEMIS observations of 605 tangential discontinuity-driven foreshock bubbles. Geophysical Research Letters, 42(19).

606

https://doi.org/10.1002/2015GL065842

- 607 Liu, T. Z., Hietala, H., Angelopoulos, V., & Turner, D. L. (2016). Observations of a new
- foreshock region upstream of a foreshock bubble's shock. Geophysical Research Letters,
- 609 43(10). https://doi.org/10.1002/2016GL068984
- 610 Liu, T. Z., Angelopoulos, V., Hietala, H., & Wilson, L. B. (2017). Statistical study of particle
- acceleration in the core of foreshock transients. *Journal of Geophysical Research: Space*
- 612 *Physics*, 122(7), 7197–7208. https://doi.org/10.1002/2017JA024043
- 613 Liu, T. Z., Lu, S., Angelopoulos, V., Lin, Y., & Wang, X. Y. (2018). Ion Acceleration Inside
- Foreshock Transients. *Journal of Geophysical Research: Space Physics*, 123(1).
- 615 https://doi.org/10.1002/2017JA024838
- 616 Liu, T. Z., Angelopoulos, V., & Lu, S. (2019). Relativistic electrons generated at
- Earth {\textquoteright}s quasi-parallel bow shock. *Science Advances*, 5(7).
- 618 https://doi.org/10.1126/sciadv.aaw1368
- 619 Liu, T. Z., Lu, S., Turner, D. L., Gingell, I., Angelopoulos, V., Zhang, H., Artemyev, A., &
- Burch, J. L. (2020a). Magnetospheric Multiscale (MMS) Observations of Magnetic
- Reconnection in Foreshock Transients. Journal of Geophysical Research: Space Physics,
- 622 125(4). https://doi.org/10.1029/2020JA027822
- 623 Liu, T. Z., An, X., Zhang, H., & Turner, D. (2020b). Magnetospheric Multiscale Observations of
- Foreshock Transients at Their Very Early Stage. *The Astrophysical Journal*, 902(1), 5.
- 625 https://doi.org/10.3847/1538-4357/abb249

- 626 Liu, T. Z., Zhang, H., Wang, C.-P., Angelopoulos, V., Vu, A., Wang, X., & Lin, Y. (2021).
- Statistical study of foreshock transients in the midtail foreshock. Journal of Geophysical
- Research: Space Physics, 126, e2021JA029156. https://doi.org/10.1029/2021JA029156
- 629 Liu, T. Z., Zhang, H., Turner, D., Vu, A., & Angelopoulos, V. (2022). Statistical study of
- favorable foreshock ion properties for the formation of hot flow anomalies and foreshock
- bubbles. Journal of Geophysical Research: Space Physics, 127, e2022JA030273.
- https://doi.org/10.1029/2022JA030273
- 633 Liu, T. Z., Vu, A., Zhang, H., An, X., & Angelopoulos, V. (2023a). Modeling the Expansion
- Speed of Foreshock Bubbles. *Journal of Geophysical Research: Space Physics*, 128(2),
- e2022JA030814. https://doi.org/https://doi.org/10.1029/2022JA030814
- 636 Liu, T. Z., Angelopoulos, V., Vu, A., & Zhang, H. (2023b). Foreshock Ion Motion Across
- Discontinuities: Formation of Foreshock Transients. *Journal of Geophysical Research*:
- 638 *Space Physics*, *128*(4), e2022JA031161.
- https://doi.org/https://doi.org/10.1029/2022JA031161
- 640 Liu, T. Z., Vu, A., Angelopoulos, V., & Zhang, H. (2023c). Analytical Model of Foreshock Ion
- Interaction With a Discontinuity: A Statistical Study. *Journal of Geophysical Research*:
- 642 *Space Physics*, 128(4), e2022JA031162.
- https://doi.org/https://doi.org/10.1029/2022JA031162
- Omidi, N., & Sibeck, D. G. (2007). Formation of hot flow anomalies and solitary shocks.
- *Journal of Geophysical Research: Space Physics*, 112(1).
- 646 https://doi.org/10.1029/2006JA011663

- Omidi, N., Lee, S. H., & Sibeck, D. G. (2021). Ion Acceleration by Foreshock Bubbles. *Journal*
- of Geophysical Research: Space Physics, 126(5), e2020JA028924.
- https://doi.org/doi.org/10.1029/2020JA028924
- 650 Schwartz, S. J., Chaloner, C. P., Christiansen, P. J., Coates, A. J., Hall, D. S., Johnstone, A. D.,
- Gough, M. P., Norris, A. J., Rijnbeek, R. P., Southwood, D. J., & Woolliscroft, L. J. C.
- 652 (1985). An active current sheet in the solar wind. *Nature*, 318(6043).
- https://doi.org/10.1038/318269a0
- 654 Schwartz, S. J., Paschmann, G., Sckopke, N., Bauer, T. M., Dunlop, M., Fazakerley, A. N., &
- Thomsen, M. F. (2000). Conditions for the formation of hot flow anomalies at Earth's bow
- shock. Journal of Geophysical Research: Space Physics, 105(A6), 12639–12650.
- https://doi.org/10.1029/1999ja000320
- 658 Schwartz, S. J., Avanov, L., Turner, D., Zhang, H., Gingell, I., Eastwood, J. P., Gershman, D. J.,
- Johlander, A., Russell, C. T., Burch, J. L., Dorelli, J. C., Eriksson, S., Ergun, R. E., Fuselier,
- S. A., Giles, B. L., Goodrich, K. A., Khotyaintsey, Y. V. Lavraud, B., Lindqvist, P., ...
- Wilder, F. (2018). Ion Kinetics in a Hot Flow Anomaly: MMS Observations. *Geophysical*
- Research Letters, 45(21). https://doi.org/10.1029/2018GL080189
- 663 Sibeck, D. G., Borodkova, N. L., Schwartz, S. J., Owen, C. J., Kessel, R., Kokubun, S., Lepping,
- R. P., Lin, R., Liou, K., Lühr, H., McEntire, R. W., Meng, C.-I., Mukai, T., Nemecek, Z.,
- Parks, G., Phan, T. D., Romanov, S. A., Safrankova, J., Sauvaud, J.-A., ... Zastenker, G. N.
- 666 (1999). Comprehensive study of the magnetospheric response to a hot flow anomaly.

- Journal of Geophysical Research: Space Physics, 104(A3).
- https://doi.org/10.1029/1998JA900021
- 669 Swift, D. W. (1995). Use of a hybrid code to model the Earth's magnetosphere. *Geophysical*
- 670 Research Letters, 22(3). https://doi.org/10.1029/94GL03082
- 671 Swift, D. W. (1996). Use of a Hybrid Code for Global-Scale Plasma Simulation. *Journal of*
- 672 *Computational Physics*, 126(1). https://doi.org/10.1006/jcph.1996.0124
- Thomas, V. A., Winske, D., Thomsen, M. F., & Onsager, T. G. (1991). Hybrid simulation of the
- formation of a hot flow anomaly. *Journal of Geophysical Research*, 96(A7).
- https://doi.org/10.1029/91JA01092
- Turner, D. L., Wilson, L. B., Liu, T. Z., Cohen, I. J., Schwartz, S. J., Osmane, A., Fennell, J. F.,
- Clemmons, J. H., Blake, J. B., Westlake, J., Mauk, B. H., Jaynes, A. N., Leonard, T., Baker,
- D. N., Strangeway, R. J., Russell, C. T., Gershman, D. J., Avanov, L., Giles, B. L., ...
- Burch, J. L. (2018). Autogenous and efficient acceleration of energetic ions upstream of
- Earth's bow shock. *Nature*, 561(7722), 206–210. https://doi.org/10.1038/s41586-018-0472-
- 681 9
- Vu, A., Liu, T. Z., Zhang, H., & Delamere, P. (2022). Hybrid Simulations of a Tangential
- Discontinuity-Driven Foreshock Bubble Formation in Comparison With a Hot Flow
- Anomaly Formation. Journal of Geophysical Research: Space Physics, 127(6),
- 685 e2021JA029973. https://doi.org/https://doi.org/10.1029/2021JA029973

- 686 Vu, A., Liu, T. Z., Zhang, H., & Delamere, P. (2023). Parameter Dependencies of Early-Stage 687 Tangential Discontinuity-Driven Foreshock Bubbles in Local Hybrid Simulations. Journal 688 of Geophysical Research: Space Physics, 128(2), e2022JA030815. 689 https://doi.org/https://doi.org/10.1029/2022JA030815 690 Vu, A. (2023a). 2.5-D Local Hybrid Simulations of Hot Flow Anomalies Under Various 691 Magnetic Field Geometries (Version 3) [Dataset]. figshare. 692 https://doi.org/10.6084/m9.figshare.23895945.v3 693 Vu, A. (2023b). 2.5-D Local Hybrid Simulations of Discontinuity-Driven Compressional 694 Boundaries Under Various Magnetic Field Geometries (Version 2) [Dataset]. figshare. 695 https://doi.org/10.6084/m9.figshare.24588921.v2 696 Vu, A., Liu, T. Z., Angelopoulos, V., & Zhang, H. (2024). 2.5-D Local Hybrid Simulations of 697 Discontinuity-Driven Compressional Boundaries Under Various Magnetic Field 698 Geometries. Submitted to JGR. 699 Wang, B., Liu, T., Nishimura, Y., Zhang, H., Hartinger, M., Shi, X., Ma, Q., Angelopoulos, V.,
- & Frey, H. U. (2020). Global propagation of magnetospheric Pc5 ULF waves driven by
 foreshock transients. *Journal of Geophysical Research: Space Physics*, 125(12).
 Wang, B., Zhang, H., Liu, Z., Liu, T., Li, X., & Angelopoulos, V. (2021). Energy Modulations of
 Magnetospheric Ions induced by Foreshock Transient-Driven ULF Waves. *Geophysical*

Research Letters.

- Wang, S., Q.-G. Zong, and H. Zhang (2013), Hot flow anomaly formation and evolution: Cluster
- observations, J. Geophys. Res. Space Physics, 118, 4360–4380, doi:10.1002/jgra.50424.
- Wilson, L. B., Sibeck, D. G., Turner, D. L., Osmane, A., Caprioli, D., & Angelopoulos, V.
- 708 (2016). Relativistic Electrons Produced by Foreshock Disturbances Observed Upstream of
- Earth's Bow Shock. *Physical Review Letters*, 117(21).
- 710 https://doi.org/10.1103/PhysRevLett.117.215101
- 711 Zhang, H., Sibeck, D. ~G., Zong, Q.-G., Gary, S. ~P., McFadden, J. ~P., Larson, D., Glassmeier,
- 712 K.-H., & Angelopoulos, V. (2010). Time History of Events and Macroscale Interactions
- during Substorms observations of a series of hot flow anomaly events. *Journal of*
- 714 Geophysical Research: Space Physics, 115(A14), A12235.
- 715 https://doi.org/10.1029/2009JA015180
- Zhang, H., Zong, Q., Connor, H., Delamere, P., Facskó, G., Han, D., Hasegawa, H., Kallio, E.,
- Kis, Á., Le, G., Lembège, B., Lin, Y., Liu, T., Oksavik, K., Omidi, N., Otto, A., Ren, J.,
- Shi, O., Sibeck, D., & Yao, S. (2022). Dayside Transient Phenomena and Their Impact on
- the Magnetosphere and Ionosphere. Space Science Reviews, 218(5), 40.
- 720 https://doi.org/10.1007/s11214-021-00865-0
- 721 Zhao, L. L., H. Zhang, and Q.-G. Zong (2017), A statistical study on hot flow anomaly current
- sheets, J. Geophys. Res. Space Physics, 122, 235–248, doi:10.1002/2016JA023319.